Geochemistry, Geophysics, Geosystems

RESEARCH ARTICLE
10.1029/2020GC009305

Thermal and Compositional Anomalies of the Australian Upper Mantle From Seismic and Gravity Data

Magdala Tesauro[1,2], **Mikhail K. Kaban**[3,4], **and Alan R. A. Aitken**[5]

[1]Dipartimento di Matematica e Geoscienze, Università di Trieste, Trieste, Italy, [2]Department of Earth Sciences, Utrecht University, Utrecht, The Netherlands, [3]GFZ German Research Centre for Geosciences, Potsdam, Germany, [4]Schmidt Institute of Physics of the Earth, Moscow, Russia, [5]School of Earth Sciences, The University of Western Australia, Perth, WA, Australia

Key Points:
- A thermo-compositional model of the Australian lithosphere is constructed
- The West and North Australian cratons have a thick, cool, and depleted lithosphere
- Hot and more fertile lithosphere is present beneath the eastern Australian margin

Supporting Information:
- Figure S1

Correspondence to:
M. Tesauro,
mtesauro@units.it

Citation:
Tesauro, M., Kaban, M. K., & Aitken, A. R. A. (2020). Thermal and compositional anomalies of the Australian upper mantle from seismic and gravity data. *Geochemistry, Geophysics, Geosystems*, *21*, e2020GC009305. https://doi.org/10.1029/2020GC009305

Received 20 JUL 2020
Accepted 21 SEP 2020
Accepted article online 25 SEP 2020

Abstract To discern temperature and compositional variations of the Australian upper mantle, we apply an integrative technique, which jointly interprets seismic tomography and gravity data. The final thermal model, obtained by changing the upper mantle composition according to the density variations, shows temperatures higher by 100–150°C in the Archean and Proterozoic upper mantle, with respect to the initial model based on a uniform "fertile" composition. In the North and West Australian cratons, the upper mantle is cold, with composition depleted in heavy constituents. This suggests the presence of an Archean lithosphere, which remained relatively undisturbed through the Proterozoic. Central Australia is predominantly characterized by a thick, low-temperature lithosphere having a more fertile composition. Its shallow part is characterized by a thin layer of low-velocity mantle, which is interpreted by our results as a thermal anomaly. However, this high-temperature anomaly is hard to reconcile with the tectonic history of the region. A low-density mineral phase, such as amphibole, may reduce the density relative to our assumed composition. Furthermore, we observe larger iron depletion in the Western Australian Craton than in the Proterozoic terranes. At the depths larger than 150 km, the depletion becomes negligible beneath the Proterozoic regions, while it also persists in the Western Australian Craton at the depths larger than 200 km.

1. Introduction

Since the Archean, the Australian Continent has evolved through different tectonic processes (Aitken et al., 2016; Betts et al., 2002; Cawood & Korsch, 2008), and these are associated with different thermal and compositional effects on the Australian lithosphere. Changes in time include secular changes in the global tectonic system (Brenhin Keller & Schoene, 2012; Brown, 2007; Groves et al., 2005; Reddy & Evans, 2009; Van Kranendonk & Kirkland, 2016) and the specific character of different tectonic periods, such as periods more or less dominated by accretionary tectonics, rifting, and mantle plume activity associated with supercontinent cycles (Condie, 2004; Murphy & Nance, 2012; Nance et al., 2014; Rogers & Santosh, 2003; Santosh et al., 2009). In particular, the Archean lithosphere is associated with intense melt extraction events that have strongly depleted it and generated long-lived and buoyant lithospheric cores (Griffin et al., 2009).

The Australian continental crust has an overall westward age progression from dominantly Phanerozoic in the east, dominantly Proterozoic in the center and dominantly Archean in the west (Figure 1). Previous lithospheric scale studies have recognized changes in the lithospheric thickness and physical properties (temperature and composition), according to fundamental boundaries at 140–145°E and 120–125°E (Aitken et al., 2015; Fishwick et al., 2005, 2008; Hoggard et al., 2020; Kennett et al., 2004; Yoshizawa, 2014; Yoshizawa & Kennett, 2015). However, these boundaries do not clearly define thermal and compositional trends, nor a clear distinction between Archean and Proterozoic lithospheres.

Up to now, several geophysical and petrological studies (e.g., Chopping & Kennett, 2015; Goes et al., 2005; O'Really et al., 1997) have identified first-order temperature variations in the Australian Continent. Using magnetic data, Chopping & Kennett (2015) found that Archean and Proterozoic provinces have the largest depths to the base of magnetization between 55 and 80 km, indicating relatively low geothermal gradients in these areas. Goes et al. (2005) identified an average trend of increasing temperature with decreasing thermo-tectonic age and a large thermal variability (200–700°C), by inverting *S-velocity* models into mantle temperatures. Xenoliths data revealed thermal perturbations associated with volcanic episodes in Eastern

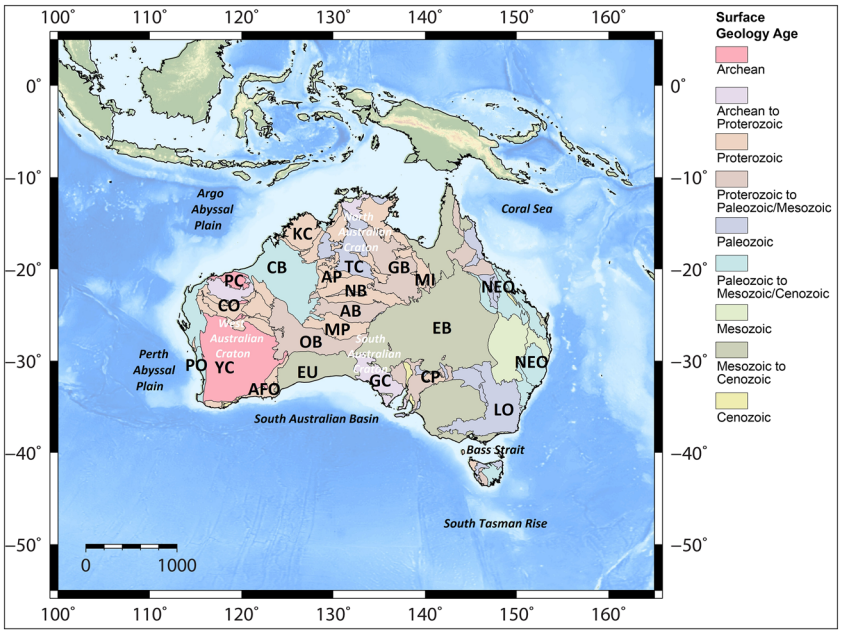

Figure 1. Age of the crystalline crust of the Australian Continent (modified after Aitken et al., 2015). Red labels show the abbreviations of the names of the main tectonic provinces as follows: *West Australian Craton*: PC, Pilbara Craton; YC, Yilgarn Craton; CO, Capricorn Orogen. *South Australian Craton*: CP, Curnamona Province; GC, Gawler Craton. *North Australian Craton*: AP, Arunta Province; KC, Kimberley Craton; MI, Mt. Isa Inlier. *Proterozoic Orogens*: AFO, Albany–Fraser Orogen; MP, Musgrave Province; TC, Tennant Creek. *Phanerozoic Orogens*: LO, Lachlan Orogen; NEO, New England Orogen; NEQ, North East Queensland; PO, Pinjarra Orogen. *Major Sedimentary Basins*: EU, Eucla Basin; OB, Officer Basin; AB, Amadeus Basin; CB, Canning Basin; NB, Ngalia Basin; GB, Georgina Basin; EB, Eromanga Basin.

Australia, while the Archaean and Proterozoic areas in Western Australia show typically low temperatures (Hoggard et al., 2020; O'Really et al., 1997). Joint interpretation of the thermo-compositional structure of the Australian Continent has been recently made by Khan et al. (2013), who applied a Markov Chain Monte Carlo method, using the global surface wave phase-velocity maps of Visser et al. (2008). These results showed that the old central and western Archean and Proterozoic regions have a cold upper mantle up to a depth of 250 km, characterized by high Mg/Fe and Mg/Si values relative to the eastern Phanerozoic part and oceanic regions. On the other hand, the statistical approach, which was employed by Khan et al. (2013), allowed to estimate uncertainties of the inverted parameters but has the problem with the nonuniqueness of the solution.

This study seeks to resolve the thermo-compositional structure of the Australian upper mantle. We discern temperature and compositional variations of the Australian upper mantle, by applying an integrative technique that jointly interprets seismic tomography and gravity data (Kaban, Tesauro, et al., 2014; Tesauro et al., 2014a). Even though the results might be affected by some uncertainties of the input parameters, they made it possible to identify the main physical characteristics of the tectonic provinces of the Australian Continent, helping better define their past and present development.

2. Tectonic Setting

To first order, Precambrian Australia has been divided into three main Archean cratons: the West, North, and South Australian cratons (Myers et al., 1996), which are separated from each other by Proterozoic orogenic belts and/or Phanerozoic sedimentary basins (Aitken et al., 2016; Betts et al., 2002; Cawood & Korsch, 2008). Although some highly juvenile suites exist, many of the Proterozoic orogens share an isotopic history with their adjacent cratons (Hollis et al., 2013; Kirkland et al., 2011, 2013), suggesting that, in general, these Proterozoic orogens involved reworking of older lithosphere, rather than the generation of entirely new lithosphere. The Precambrian lithosphere mostly remained tectonically stable up to ~1,290 Ma. After

this time, it was modified by a number of tectonic events, including the formation of large igneous provinces (LIPs), orogens, rifts, and widespread basin (Aitken et al., 2016).

The West Australian Craton (WAC) comprises the Pilbara and Yilgarn cratons, whose amalgamation, occurred through a series of Palaeoproterozoic events from 2,200 to ~1,950 Ma, leads to the formation of the Capricorn Orogen (Johnson et al., 2011). This orogen was subsequently reactivated during the Neoproterozoic. The North Australian Craton (NAC) is composed of several different blocks, including the Kimberley Craton in the northwest, the Tennant Creek Inlier in the center, the Mt. Isa Inlier to the east, and the Arunta Inlier on the southern margin. With the exception of the Arunta Inlier, the NAC escaped major reworking in the Meso-Neoproterozoic period. The South Australian Craton (SAC) consists of the Gawler Craton in the center and west and the Curnamona Province in the east (Betts et al., 2002). The Gawler Craton is composed of an Archean terrane folded into an orocline, with a central late Paleoproterozoic magmatic arc (St. Peters Suite). Basement in the Curnamona Province is not exposed but is likely related to the NAC terranes (Betts et al., 2016). Both these regions were affected by intense magmatism during the early Mesoproterozoic Hiltaba Event.

Australia was a component of different supercontinents, such as Nuna/Columbia and Gondwana, when substantial crustal growth occurred, including 1,800–1,400 Ma accretionary margins, now located in central Australia (Aitken et al., 2016) and the Tasmanides of Eastern Australia (ca. 550–250 Ma) (Cawood, 2005). To the Rodinian-era orogens belong the Musgrave and Albany-Fraser orogenies and Warakurna LIP (Aitken et al., 2016). During this time, there was no significant crustal growth in Australia, but rather extensive reworking of older lithosphere, resulting in lithospheric mantle rejuvenation and substantial crustal modification (Alghamdi et al., 2018; Smithies et al., 2011).

Following the amalgamation of the cratonic blocks, the central region of Australia continued to be subjected to intraplate orogenic activity. This included substantial Grenville-era activity in central and southern Australia (the Albany-Fraser and Musgrave orogenies) and the subsequent rifting and magmatic event (the Giles Event and Warakurna LIP) in central and west Australia. During the Neoproterozoic, the supercontinent Rodinia brokeup (~800 Ma), and the Centralian Superbasin (Amadeus, Ngalia, Georgina, and Officer basins) developed in central Australia (Walter et al., 1995), likely as a result of extension and thinning of the lithosphere, caused by the upwelling of a mantle plume located on the eastern edge of the Gawler Craton (Zhao et al., 1994).

The Phanerozoic Tasmanides in the east of Australia were accreted onto the eastern margin of the Precambrian craton in a series of stages from the late Neoproterozoic to the early Triassic (Cawood, 2005; Direen & Crawford, 2003; Glen, 2005; Rosenbaum, 2018). These origins are dominated by supracrustal successions, deposited upon extended crust. Potentially, the underlying crust and lithosphere are Proterozoic, at least to ~140°E (Fishwick et al., 2008). In the Mesozoic, southeastern Australia was the continental margin of the subducting Pacific Plate (Fontaine et al., 2013). Since 40 Ma, Eastern Australia was affected by significant volcanism, with eruptions as recent as 4000 BC at Mt. Gambier, which left an age progressive of the volcano chains on land and in the Tasman Sea (Kennett et al., 2017).

3. Present-Day Crust and Upper Mantle Structure

The crust and upper mantle of Australia have been investigated in the last two decades using a variety of geophysical methods, mainly seismic tomography (Fichtner et al., 2010; Fishwick et al., 2005, 2008; Fishwick & Rawlinson, 2012; Fishwick & Reading, 2008; Kennett et al., 2004, 2013; Salmon et al., 2013; Yoshizawa, 2014; Yoshizawa & Kennett, 2015) also supplemented by gravity and magnetic studies (Aitken et al., 2015; Chopping & Kennett, 2015).

We can observe that the topography of Australia is lower than the other tectonic plates on average: it is low to moderate in the north and west and very low in the south-central region. More elevated topographies are visible along the eastern and southeastern margins (Figure 2a). The sedimentary thickness, reconstructed by Salmon et al. (2013), reaches the greatest values offshore (>15 km), along the northwestern and southern margins (Figure 2b). In the continental regions, large thickness of sediments (up to 10 km) is observed in the Centralian Superbasin, Eromanga, and Canning basins. The Moho depth in the Australian Continent according to the Australian Seismological Reference Model (AuSREM; Kennett et al., 2013, http://rses.

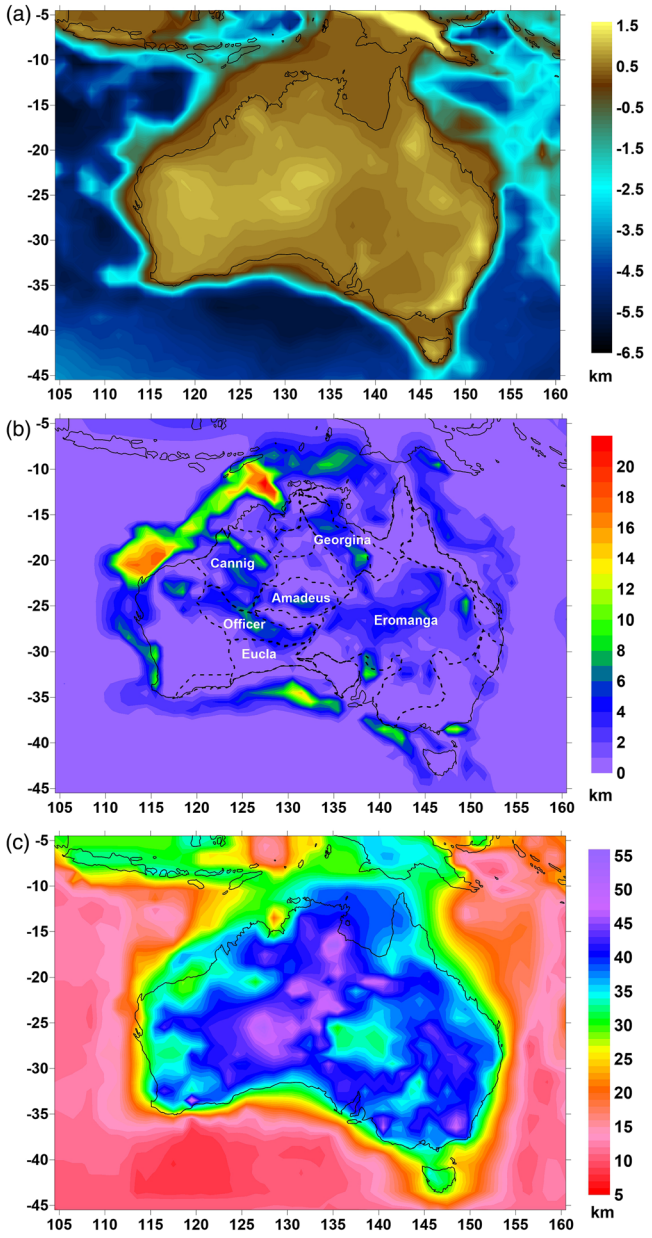

Figure 2. Crustal structure of the Australian Continent and initial gravity model. (a) Topography; (b) Sedimentary thickness. White labels show the names of the main continental sedimentary basins; (c) Moho depth. The data are provided by AuSREM (http://rses.anu.edu.au/seismology/AuSREM/index.php).

anu.edu.au/seismology/AuSREM/index.php) varies between 30 and 55 km except for the continental margins characterized by thinned crust (Figure 2c). In Western Australia, beneath the Pilbara and Yilgarn cratons, the crust is mostly thin (30–35 km), and the Moho represents a sharp clearly outlined boundary (e.g., Clitheroe et al., 2000; Yuan, 2015). The thickness, density, and Vp/Vs ratio of the crust clearly depend on age, which is associated with secular crustal evolution (Yuan, 2015). The Moho beneath the Yilgarn Craton becomes deeper (~40 km) and more diffusive along its eastern and southern margins and further deepens beneath the Capricorn Orogen (>40 km). The thickest crust in Australia occurs in the NAC, in central Australia, and in parts of southeast Australia, where the largest depth is observed. In these regions, the Moho likely represents gradual crust-mantle transition zone (2–10 km wide) rather than a sharp boundary, which has been interpreted as a result of underplating at the base of the crust (Clitheroe et al., 2000). This thick crust is typically dense (Aitken et al., 2013) and the associated underplating is likely due to the large-scale mafic-dominated magmatic events (Alghamdi et al., 2018). Toward Eastern Australia, Tasmania, and the Bass Strait, we observe a rapid transition to a much thinner crust (30 km on average), likely resulting from the Gondwana breakup. The large difference in the crustal thickness between the Proterozoic NAC and the eastern Phanerozoic regions can be related to the presence of the underplating of mafic and ultramafic rocks in the former regions. This hypothesis is supported by the systematic increase of the Poisson ratio associated with the increase of the crustal thickness in the Proterozoic areas (Chevrot & van der Hilst, 2000). In contrast, the Poisson coefficient of the Phanerozoic crust tends to decrease with increasing crustal thicknesses, due to higher proportion of the felsic crustal component.

Seismic tomography studies revealed the most robust large-scale features of the continental lithosphere of Australia, including the Archean and Proterozoic cratons and Proterozoic lithosphere beneath the western Tasmanides (Fichtner et al., 2010; Fishwick & Rawlinson, 2012; Fishwick & Reading, 2008; Rawlinson et al., 2014; Yoshizawa, 2014; Yoshizawa & Kennett, 2015). Slow wave speeds have been observed in the lithospheric mantle underneath the eastern and southeastern margins (Fishwick & Rawlinson, 2012; Rawlinson et al., 2014; Yoshizawa, 2014; Yoshizawa & Kennett, 2015). Several studies have identified an area of low seismic velocities in the uppermost mantle beneath central Australia, with high radial anisotropy (Fichtner et al., 2010; Fishwick & Rawlinson, 2012; Fishwick & Reading, 2008). This zone of slow wavespeeds is underlain by a region of fast wavespeeds, more typical of continental lithosphere. This layered velocity structure has been interpreted to be of thermal origin, due to the redistribution of high heat producing elements within the crust (e.g., Goes et al., 2005), but it can also be the effect of composition, in particular the presence of low-density mineral phases (e.g., amphibole; Fishwick & Reading, 2008). To resolve these controversies and reduce ambiguity in interpreting seismic velocity anomalies, it is necessary to know thermo-compositional structure of the upper mantle.

4. Data Input

4.1. Seismic Tomography Data

For the purpose of this study, we used the AuSREM model, which provides *S* and *P* wavespeed distributions through the crust from 5- to 60-km depth, with a step of 5 km, and upper mantle, from 50- to 300-km depth,

with a step of 25 km. The lateral resolution is 0.5° both in latitude and longitude. The model was obtained by a combination of previous models, based on different methods, including ambient noise tomography for the crust (Kennett et al., 2013; Kennett & Salmon, 2012; Salmon et al., 2013). The crustal component of the model is also based on prior compilations of the sedimentary thickness and of all available seismic data of the Moho depth (Salmon et al., 2013). To perform the gravity calculations on a global scale, we embedded the regional AuSREM model in the global *S*-wave tomography model for the mantle (SL2013sv) of Schaeffer and Lebedev (2013), developed using the partitioned waveform inversion technique (Nolet, 1990). This model provides *Vs* values from the depth of 56–720 km, with a lateral resolution of 0.5° and variable vertical resolution (50 km on average). The integration of the regional AuSREM model with the global SL2013sv allowed to model deep density structure, for which we need to consider far-field effects that can significantly influence the gravity field. Furthermore, the iterative method applied to distinguish thermal and compositional anomalies is based on decomposition in spherical harmonics, which also require global coverage. Despite the data outside, the study area might be less reliable and could vary in different tomography models; for far-field effects, we should consider only very large/wide structures (like Pacific or Eurasia), which are sufficiently consistent in most of the global models. For the crustal structure outside the Australian Plate, we used the model CRUST1.0 (Laske et al., 2013), which has been improved based on recent continental wide studies of North America (Tesauro et al., 2014b), Eurasia (Stolk et al., 2013; Tesauro et al., 2008), and Antarctica (Haeger et al., 2019).

One of the principal problems for our modeling is the possible reduction of the amplitude of seismic velocity anomalies due to damping. Root (2020) suggested to scale the initial tomography model by making the spectrum of its gravity effect similar to the spectrum of the residual mantle gravity field. This approach is efficient on a global scale, as it was done by Root (2020). However, we think that it is dangerous to apply it in our case. The mantle gravity field in Australia substantially depends on compositional variations, which only marginally affect seismic velocities. Therefore, its spectrum is naturally higher than of the initial model based on tomography. On the other hand, the actual damping of the regional AuSREM model is likely much less than of the global model, due to incomparably denser data coverage. Therefore, the reduction of the amplitude should not be significant.

We display the AuSREM model used in this study in terms of *S*-wave velocity variations at the depth of 100 km and along four cross sections in Figure 3. One can observe a broad zone of high velocities localized in the WAC and NAC and a smaller area of low velocities in Eastern Australia. The greatest velocity values (>4.7 km/s) at 100 km are observed in the Yilgarn and Pilbara cratons, which clearly distinguish from the Capricorn Orogen. High velocities (~4.7 km/s) extend beneath the WAC down to a depth of 300 km (Figure 3, cross sections A-A′, B-B′, and C-C′). In contrast, the southern part of the NAC (e.g., Amadeus Basin) shows low velocities (~4.5 km/s) in the shallow upper mantle (<120 km), which sharply increase (to >4.7 km/s) at larger depths. As discussed in section 3, the origin of the low velocities (thermal or compositional) is still unresolved. In contrast to the NAC and WAC, the SAC shows upper mantle low velocities (~4.5 km/s, Figures 3a and 3b). At ~140–145°E, a sharp velocity change is observed between the Delamerian and Lachlan orogens, which reflects a change from a continental Proterozoic mantle lithosphere to an oceanic Phanerozoic mantle lithosphere (Fishwick & Rawlinson, 2012; Rawlinson & Fishwick, 2012). The very low-velocity zone in the shallow upper mantle (~4.3 km/s at 100 km) in East Australia extends further to the East along the continental margin and southward beneath Bass Strait and Tasmania (Figure 3). This anomaly may be a result of the elevated temperatures related to the breakup of Australia and Antarctica with the consequent opening of the Tasman Sea and the Southern Ocean (~95 Ma). This thermal anomaly has its surface expression in the chain of Cenozoic volcanoes, extending down to the east coast of Australia and into the southeast (Rawlinson et al., 2017). The seismic velocity anomaly disappears at depths larger than 250 km. Therefore, it has been interpreted as a result of upper mantle processes, such as edge driven convection (e.g., Fishwick & Rawlinson, 2012; Rawlinson & Fishwick, 2012).

4.2. Initial Gravity Field

As initial gravity field, we used the Eigen-6C4 model (Förste et al., 2014), which is based on a combination of satellite data (mainly from recent GRACE and GOCE satellites) and existing ground/airborne measurements (Figure 4). In this way, the satellite data provide a consistent regional field, while ground

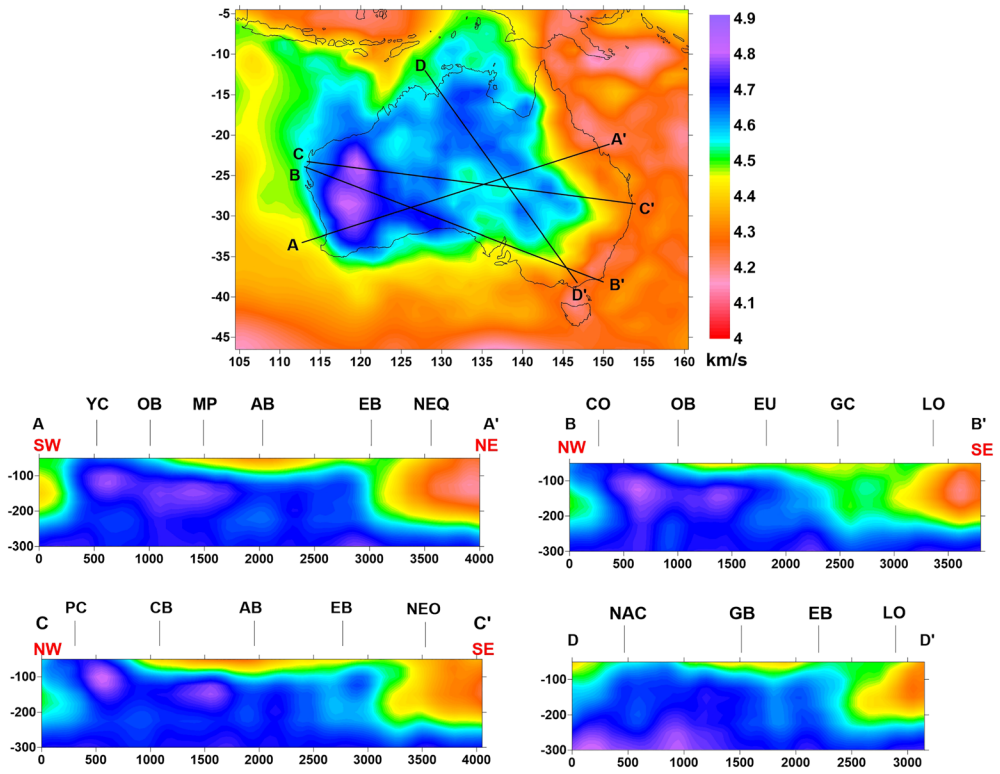

Figure 3. *S*-wave velocity (km/s) provided by AuSREM model (http://rses.anu.edu.au/seismology/AuSREM/index.php) at a depth of 100 km and along four cross sections. Black lines show the cross-sectional location and black labels, on the top of the cross sections, the abbreviations of the names of the main tectonic provinces displayed in Figure 1.

observations give small-scale details. The maximal resolution is ~10 km (2,190 spherical harmonics degree), which basically corresponds to the coverage of ground observations in well-sampled regions of Australia. Therefore, the resolution and accuracy of the initial gravity field are more than enough for the present study. Since the resolution of other data sets is set to 1° × 1°, the gravity field was also rescaled by averaging the initial data over 1° × 1° cells.

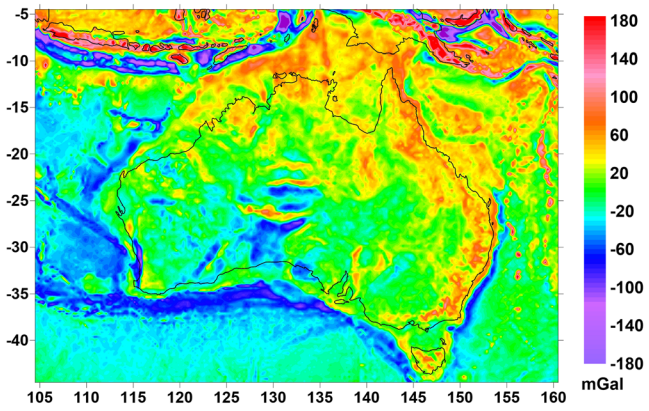

Figure 4. Initial free air disturbances of the gravity field (Eigen-6C4; Förste et al., 2014). The resolution of the initial field (approximately 2,190 spherical harmonics degree) is reduced to fit the resolution of other data and of the final model (1° × 1°).

5. Method

The method that we applied in this study (Figure 5) consists of several steps (Kaban, Tesauro et al., 2014; Tesauro et al., 2014a). First, we calculated the gravity effects of the crustal layers and removed them from the observed gravity field and topography. By this, we obtained the residual mantle gravity anomalies and residual topography (Figures 8a and 8b). Afterwards, we estimated temperature variations in the uppermost mantle (Figure 10), based on seismic tomography constrained by mineral physics (Stixrude & Lithgow-Bertelloni, 2005), without considering compositional variations. The gravity effect of temperature induced density variations was removed from the residual gravity and topography (Figure S1). Successively, these fields were inverted to obtain a 3D density model of the upper mantle, which complement the initial temperature-induced variations. The density model derived from the joint inversion was employed to estimate compositional changes, which were used in turn to recalculate the upper mantle temperatures for the next iterations, taking into account the compositional changes. These steps were repeated, allowing to refine both the upper mantle temperature and composition, until the convergence was reached. We assume that this

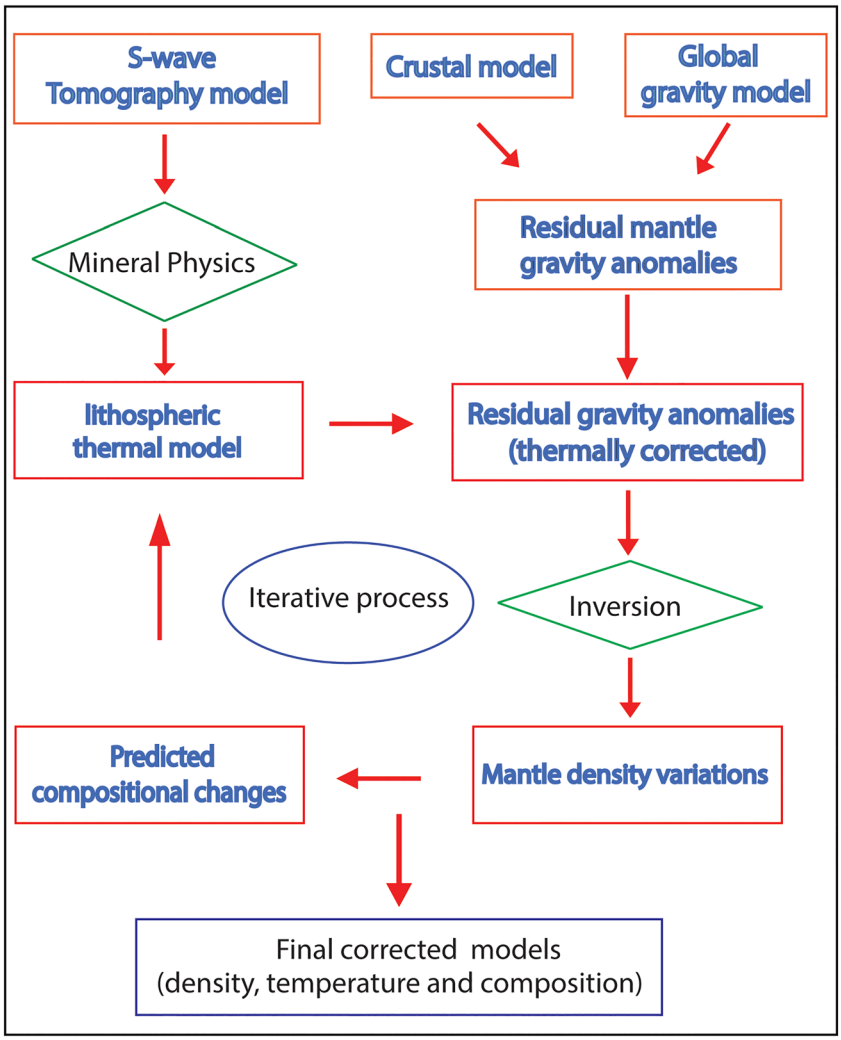

Figure 5. Workflow of the iterative technique used in this study, modified after Kaban, Tesauro et al., 2014.

occurred when the density changes after the next iteration were within 1%. Below, we describe in more details the main steps of this method.

5.1. Crustal Gravity Effect

To calculate the gravity effect of the crust, we used the crustal structure and the seismic tomography model provided by AuSREM (section 4.1).

As in previous studies, gravity anomalies induced by crustal layers were calculated from density variations in each layer relative to a 1D reference model (e.g., Mooney & Kaban, 2010). It was demonstrated that plausible variations of the reference model cause basically a constant shift of the final residual mantle anomalies. Therefore, possible changes of the reference densities do not affect the results in this study (e.g., Kaban et al., 2004). However, in order to compare directly the residual anomalies obtained for different regions, we used the reference model employed previously in global (Kaban et al., 2003; Kaban, Petrunin et al., 2014) and regional studies (Kaban et al., 2010, 2015; Kaban, Stolk, et al., 2016; Kaban, Tesauro et al., 2014; Mooney & Kaban, 2010). The density values of the crust have been obtained from Christensen and Mooney (1995) that provided the velocity-density relationships for in situ conditions, based on rocks' experiments performed at different range of T-P. The density values for the upper mantle are based on seismic tomography (Kaban et al., 2015). The reference densities are shown in Table 1.

Table 1
1D Reference Density Model of the Crust and Upper Mantle

	Depth (km)	Density (kg/m^3)
Upper crustal layer	0–15	2,700
Lower crustal layer	15–40	2,940
Upper mantle	40–75	3,320
Upper mantle	100	3,384
Upper mantle	150	3,419
Upper mantle	200	3,457

The gravity anomalies of each layer have been computed with a 3D method on a spherical Earth; the detailed description of this technique is in Kaban, El Khrepy, and Al-Arifi (2016). As stated in section 4.1, to take into account the effect of the distant zone, the model of Australia has been embedded into a the global one.

We converted the *P*-wave velocity from AuSREM into density at different depths of the sedimentary rock layer using the Gardner et al. (1974) relationship and obtained two representative density-depth curves for the offshore (less consolidated sediments) and onshore sediments (consolidated sediments), characterized by relatively high- and low-density gradients, respectively (Figure 6a). Both curves approximate crystalline rocks' density values (>2.65 g/cm^3) at a depth of about 7 km. These data have been used to estimate the anomalous gravity effect of the sedimentary basins, which spans from 0 to −100 mGal (Figure 7a). The lowest values correspond to the continental areas with the greatest thickness of sedimentary rocks.

To estimate the gravity effect of the crystalline crust, we converted the average *Vp* velocity into density, using the empirical relatonship of Christensen and Mooney (1995). Velocities, and thus densities of the crystalline crust vary in a large range (Figure 6b). Gravity anomalies, estimated with respect to the reference model (Table 1), resulting from the crystalline crust are positive in most of the continental area (Eastern Australia, NAC and SAC cratons), with the largest values (+90 mGal) in the regions of high crustal thickness and densities (Figure 7b).

Within the continental areas, the gravity anomalies generated by the Moho depth variations (Figure 7c) are strongly negative (up to −400 mGal), while in the oceans, where the crust is very thin, there are over +300 mGal.

These three calculations remove the majority of the crustal gravity signal; however, some crustal signals may remain due to uncertainties and limited resolution of the crustal density model. Furthermore, the velocity models used are interpolated in a smoothed approach, with the effect to underestimate local velocity contrasts and thus cause an undercorrection at shorter wavelengths. The velocity to density conversions are also not exact and will be an additional source of error in the model. Therefore, a possibility to correct the crustal densities is also included in the inversion of the residual mantle gravity anomalies and residual topography to compensate these uncertainties.

In the same way as the residual gravity field, we have estimated the residual topography, which represents the part of the observed topography, which is undercompensated or overcompensated by the crustal structure in the isostatic sense (Kaban et al., 2004, 2010). Therefore, a long-wavelength part of the residual topography (several hundred km or more) is induced by the mantle heterogeneity including dynamic effects of the mantle convection. A short-wavelength part of the residual topography is also influenced by deviations

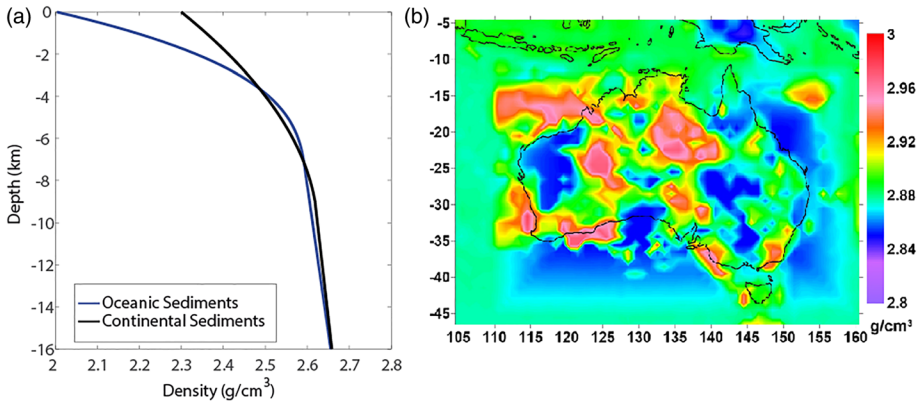

Figure 6. Crustal density variations of the Australian Continent. (a) Density-depth relationships for oceanic and continental sedimentary basins based on seismic data and (b) density of the crystalline crust.

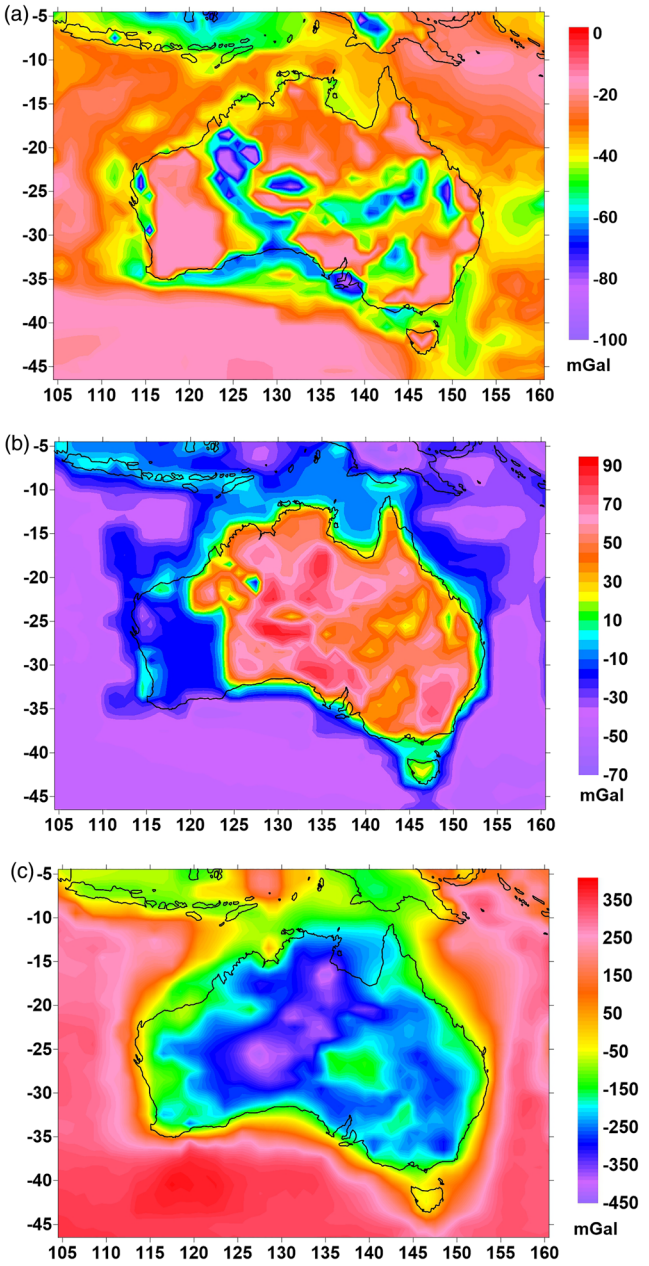

Figure 7. Gravity effect of the crustal structure. (a) Sediments; (b) crystalline crust; (c) Moho depth variations estimated relative to a standard 1D model (Table 1).

from the local isostasy, that is, by local density anomalies (including topography), which are supported by stresses in the lithosphere. Possible errors of the crustal model influence the residual topography in the same way as the residual mantle gravity anomalies (e.g., Mooney & Kaban, 2010).

5.2. Mantle Gravity Anomalies and Residual Topography

By correcting for the gravity effects of the crust, we obtained the residual mantle gravity field and residual topography (Figures 8a and 8b). In addition to the crustal correction, the effect of mantle density variations below 325 km has been estimated using a global dynamic model, as described in Kaban et al. (2015) Kaban, Stolk, et al. (2016), and removed from both residual gravity and residual topography. The depth of 325 km exceeds the potential depth of the cratonic roots; therefore, it has been chosen as the bottom of our model (Kaban et al., 2015; Kaban, Stolk, et al., 2016; Kaban, Tesauro, et al., 2014). We use the seismic tomography model of Schaeffer and Lebedev (2013) up to a depth of 720 km and the model S40rts (Ritsema et al., 2011) for the lower mantle. The velocities were converted to densities using the depth-dependent scaling factor from Steinberger and Calderwood (2006). These calculations also take into account dynamic effects of the mantle convection (Kaban et al., 2015). Therefore, these residual fields reflect the density heterogeneities of the uppermost mantle. As before explained, we undertook a joint inversion of both residual gravity and residual topography, to resolve the 3D density structure of the upper mantle.

The calculated variations of the residual mantle anomalies and residual topography over the Australian Continent are relatively small compared to other continents (e.g., Kaban, Stolk, et al., 2016; Mooney & Kaban, 2010), they span from −50 to 150 mGal and from −0.3 to +2 km, respectively (Figures 8a and 8b). In contrast, for Asia, the amplitudes of the residual mantle gravity anomalies reach ±500 mGal (Kaban et al., 2016). The obtained results evidence that the Australian mantle is characterized by relatively small total density variations compared to other continents and that possible variations of temperature may be well compensated by compositional changes.

5.3. Initial Thermal and Density Model of the Upper Mantle

We determined the thermal and corresponding density structure of the upper mantle by inverting seismic velocities as in Kaban, Tesauro et al., 2014, using the mineral physics approach of Stixrude and Lithgow-Bertelloni (2005). This approach, based on the Eularian finite strain formulation, is used to calculate synthetic velocities of the mantle mineral phases (olivine, OPX, CPX, and garnet), for a range of pressure and temperature, corresponding to the depths between 50 and 300 km. Each mineral phase is treated as an ideal solid solution of mgnesium (Mg) and iron (Fe) species (end-members) and in case of garnet also of calcium (Ca) species: olivine (forsterite + fayalite), OPX (enstatite + ferrosilite), CPX (diopside + hedenbergite), and garnet (pyrope + almandine + glossular). The percentage of the main mineral phases varies as the percentage of *Fe* and *Mg* species between two end-member compositions (expressed in mineral modes). The composition used in the initial conversion (first end-memebr) represents the fertile upper mantle, while the other (second end-memebr), used to take into account the compositional variations in the cratonic areas, represents the depleted Archean and Proterozoic upper mantle. The amount of Ca end-member of the garnet (glossular) is taken constant (20%). The parameters of each end-member at the STP conditions are taken from Stixrude and Lithgow-Bertelloni (2005).

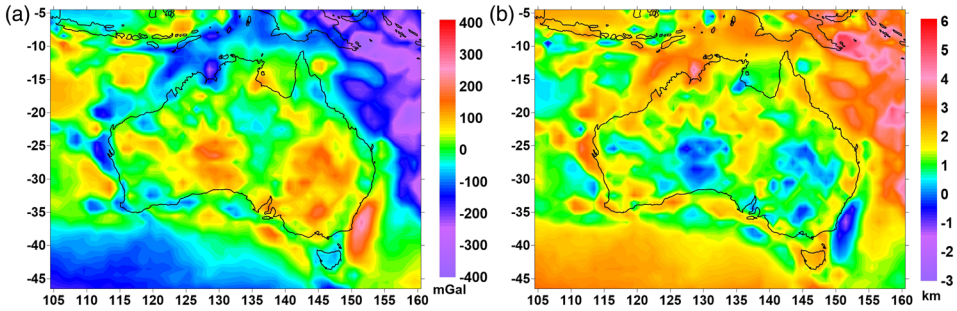

Figure 8. (a) Residual mantle gravity anomalies obtained after removal of the crustal gravity effect from the observed field. The average level is set to zero for the study area; (b) residual topography (t_{res}): the part of topography, which is noncompensated or overcompensated by the crustal structure, estimated for the density 2.67 g/cm^3. Zero level corresponds to the reference density model.

To model the upper mantle with a "fertile" composition, we used an average of the mineral fractions constituting the "primitive mantle" rock (McDonough & Sun, 1995) and the "tecton garnet peridotite" rock (Griffin et al., 2003): Ol, 58.5%; OPX, 15%; CPX, 11.5%; and Gt, 15%, with a Mg# (100 × Mg/(Mg + Fe)) = 89. The mantle temperatures were obtained comparing the seismic velocities of AuSREM model, with the synthetic anharmonic velocities, corrected for the anelasticity effect, using the attenuation model *Q4* of Cammarano et al. (2003). Although most of the continental Australia consists of cratonic areas, which suppose a high-viscosity upper mantle, we used the attenuation model *Q4*, more representative of a "wet" Phanerozoic upper mantle (Figure 9), to be consistent with the composition chosen for the first iteration. In this way, we initially assumed that *S*-wave velocity variations depend on temperature only. In the next iterations, we considered in the cratonic areas the effect of compositional variations and used an attenuation model more suitable for the "dry" conditions of the upper mantle.

5.4. Inversion of the Mantle Gravity Anomalies and Residual Topography Into Density Variations

We applied a joint inversion of the residual gravity field and residual topography, in order to modify the initial temperature-induced model of the uppermost mantle. These resulting corrections were considered to determine depletion in heavy constituents, characterizing the lithosphere in cratonic areas. In the joint inversion, we also took into account that the initial crustal model may have been biased by errors. Therefore, with an additional crustal layer, we accommodated these potential errors. The inversion procedure aims to minimize least square differences with the initial fields (g_{res} and t_{res}), while keeping minimal differences with the initial model (ρ_{ini}) (Kaban et al., 2015):

$$min\left\{\|A\rho - g_{res}\|^2 + k^2\|B\rho - t_{res}\|^2 + \alpha\|\rho - \rho_{ini}\|^2\right\} \quad (1)$$

where A and B are the operators for the gravity effect and dynamic topography induced by the density ρ, k is the scaling factor for the residual topography, and α is the damping factor.

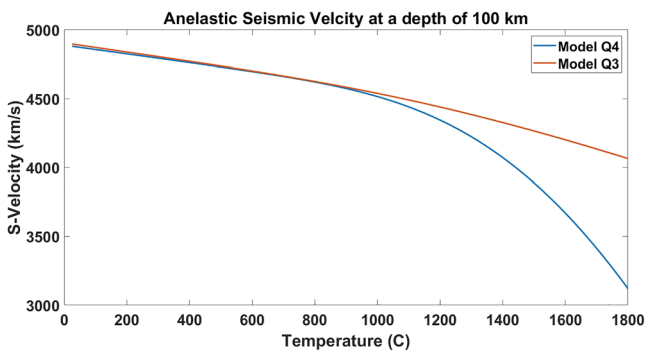

Figure 9. Syntethic seismic velocity corrected for the anelasticity model *Q3* and *Q4,* respectively.

Therefore, this is an Occam-type inversion, which requires minimal deflections from the initial densities as a precondition to regularize the solution. The inversion was performed in a spherical harmonic domain, and thus, we needed global coverage for all data sets. For the velocity variations in the upper mantle outside Australia, we employed the tomography model of Schaeffer and Lebedev (2013). The maximal horizontal resolution reaches 180°/order (1° × 1° in space domain) and the vertical resolution for the mantle is 50 km. We adjusted densities in seven layers with the central depth from 15 to 300 km. As pointed out before, the uppermost layer was introduced to allow compensation of possible errors in the crustal model, since the density of the crystalline crust is the most uncertain parameter of the initial model. The joint inversion of the residual gravity anomalies and residual topography provides a possibility to divide the effects of near surface and deep density anomalies (Kaban

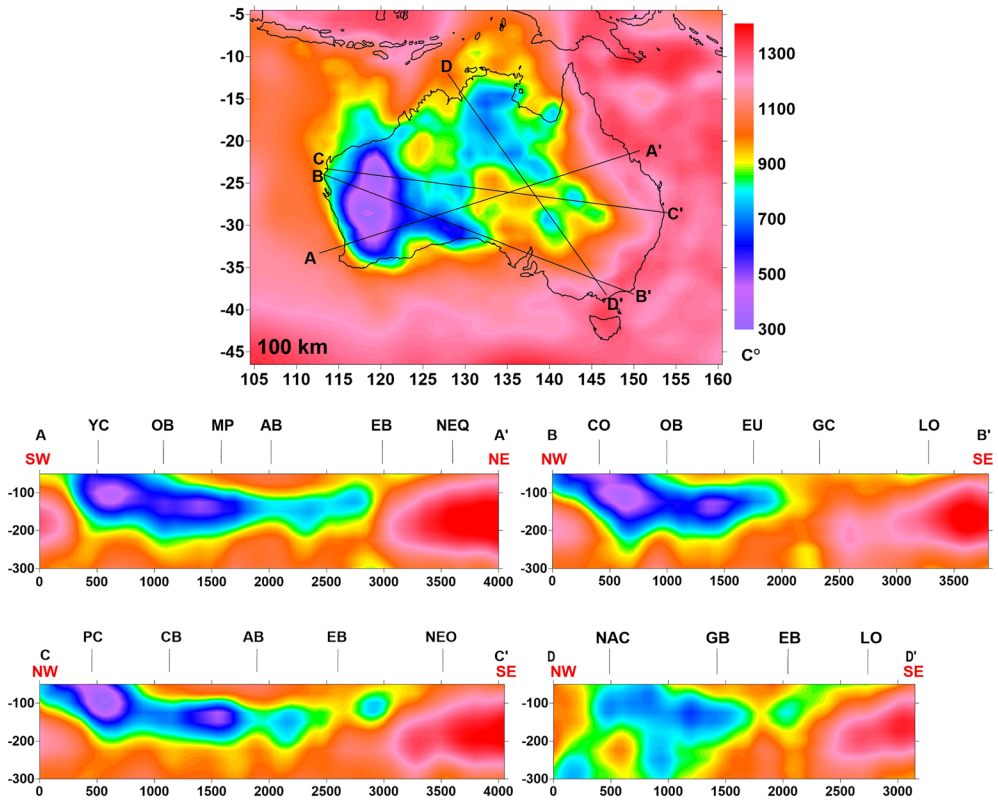

Figure 10. Temperature variations (°C) at a depth of 100 km and along four cross sections, estimated from the inversion of the regional seismic tomography model AuSREM, assuming a uniform "fertile" composition (Griffin et al., 2003; McDonough & Sun, 1995) and the anelasticity model *Q4* (Cammarano et al., 2003). Black lines show the cross-sectional location and black labels, on the top of the cross sections, the abbreviations of the names of the main tectonic provinces displayed in Figure 1.

et al., 2015). The six layers from 50 to 300 km (central depth) are related to the mantle structure. In the inversion, only density variations were determined relative to the reference densities provided in Table 1. These values correspond to the average velocity at each depth according to the Schaeffer and Lebedev (2013) tomography model converted to densities as described in section 5.3. The standard deviation of the residual gravity field and the field of the inverted model (rms) is 6.7 mGal, while the standard deviation of the residual topography is 0.06 km. These values are almost 2 orders less than the amplitude of the anomalies, indicating that the model fits well the inverted fields. It has been shown that the relative pattern and sign of density anomalies in the upper mantle are effectively restored, but the amplitudes of these anomalies may be reduced due to damping of the final solution in the inversion. Therefore, they likely represent a lower limit of the actual density variations. More details of the method and discussion of potential uncertainties can be found in Kaban et al. (2015) Kaban, Stolk, et al. (2016).

5.5. Final Thermal Model

In the cratonic areas, the final thermal model was obtained by using the upper mantle composition depleted in CPX, garnet, and *Fe* (higher Mg#), which fits the negative density variations obtained from the inversion of the residual topography and mantle gravity anomalies (section 5.4). As in Tesauro et al. (2014a), we assumed that the minimum amount of depletion, given by an increase of 0.1 in Mg# and a change in the corresponding fractions of the main mineral phases, with respect to the first end-member composition (section 5.3), is compensated by a density variation of 1.6 kg/m^3. The second end-member composition, taken from the study of Griffin et al. (2003), represents the maximum depletion that can be reached and is compatible with that of a strongly depleted Precambrian upper mantle (olivine: 69.5; OPX: 21; CPX: 4; and garnet: 5.5, with a Mg# = 94). In the cratonic areas, we also changed the attenuation model *Q4* with

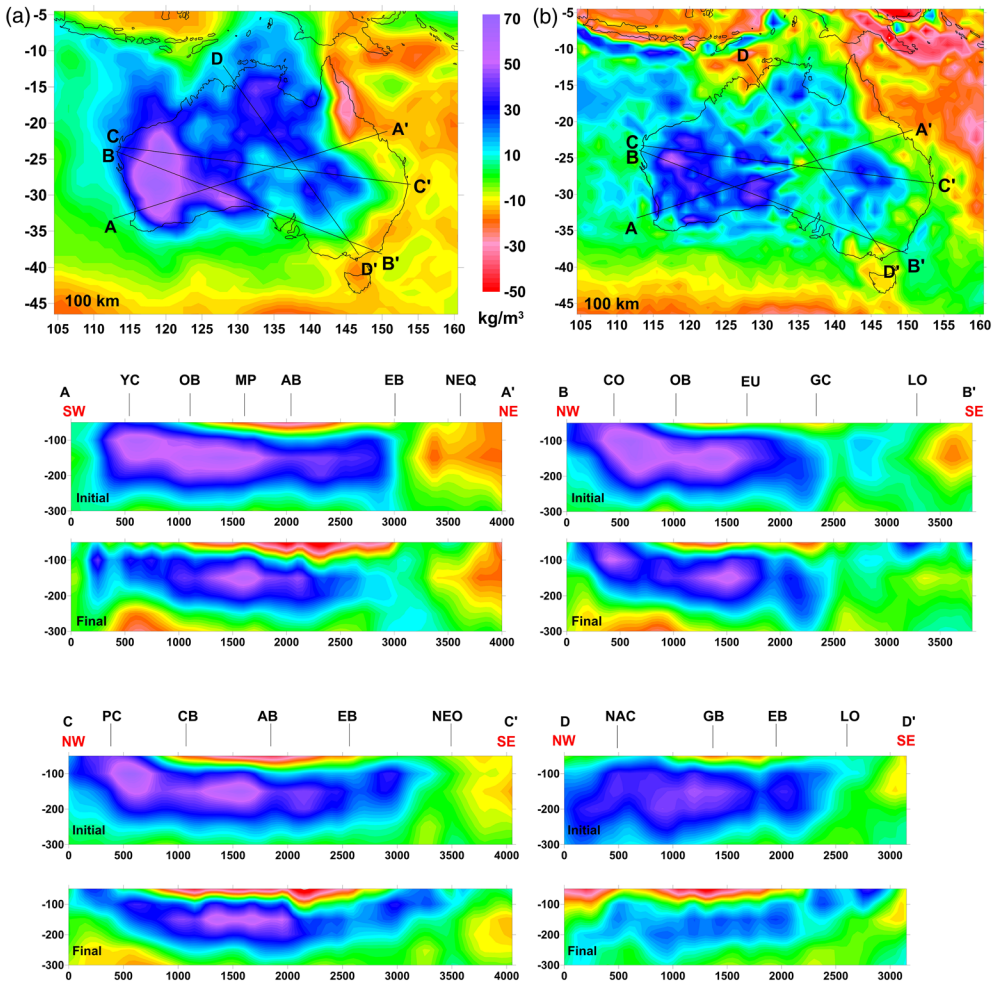

Figure 11. (a) Initial and (b) adjusted (final) density variations in the upper mantle at a depth of 100 km (kg/m^3) and along four cross sections. Black lines show the cross-sectional location and black labels, on the top of the cross sections, the abbreviations of the names of the main tectonic provinces displayed in Figure 1. (a) Initial density variations obtained from the temperature variations shown in Figure 10; (b) Adjusted density variations that fit both the residual gravity field and topography and have minimal deviations from the initial density model.

Q3 of Cammarano et al. (2003), which reduces the anelasticity effect, as expected occurring for a high-viscosity upper mantle (Figure 9).

6. Results

6.1. Initial Thermal and Density Model

We limit the discussion on the initial thermal and corresponding density models to the main features, since the model may be biased by compositional variations in the upper mantle, which significantly affect the velocity-to-temperature conversion. Therefore, we can expect an uncertainty of about 50–70 mGal for the estimated gravity effect of the mantle lithosphere (Mooney & Kaban, 2010).

The initial thermal and density models, displayed for a depth of 100 km and along four cross sections, show clear distinction among terranes of different age divided by sharp boundaries (Figures 10 and 11a). Very low temperatures (≤400°C) and strong positive density anomalies (>50 kg/m^3) are observed in the Archean-dominated WAC, as expected considering the low heat flow values (<40 mWm^{-2}). Intermediate temperatures (700–950°C) and slightly positive density anomalies (10–30 kg/m^3) are found in the Proterozoic-dominated NAC. High temperatures (>950°C) and negligible or negative density variations

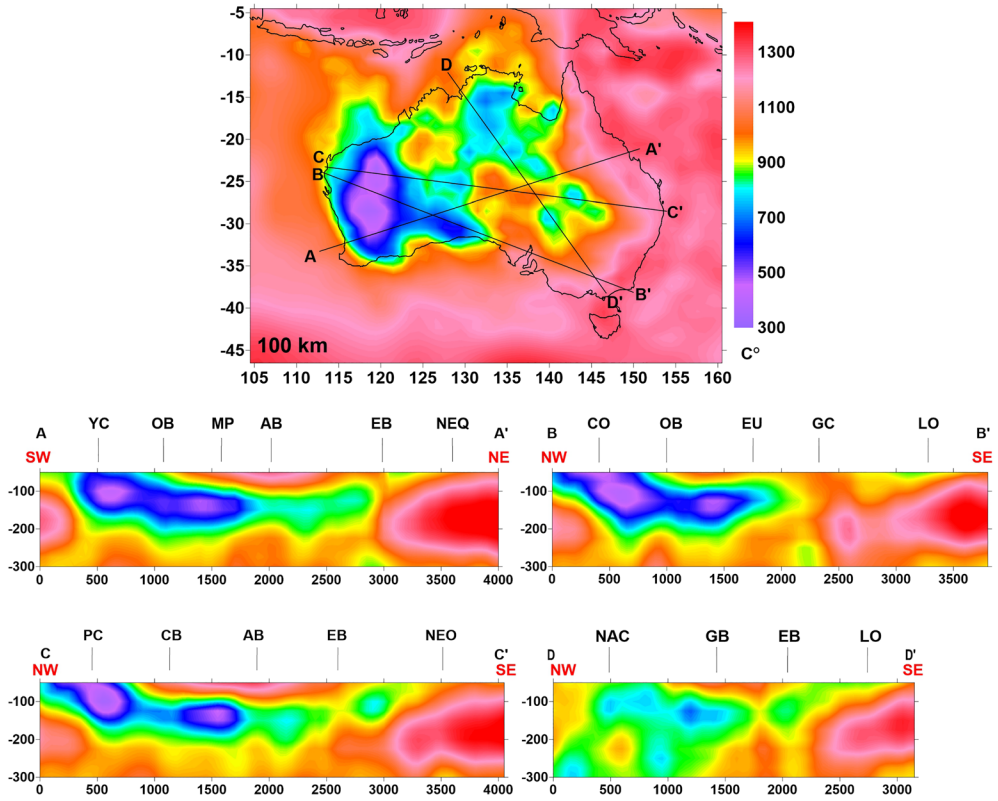

Figure 12. Temperature variations (°C) at a depth of 100 km and along four cross sections, estimated after the last iteration. Black lines show the cross-sectional location and black labels, on the top of the cross sections, the abbreviations of the names of the main tectonic provinces displayed in Figure 1.

(up to −30 kg/m^3) are visible in the Phanerozoic terranes, also characterized by medium-elevated heat flow values (60–70 mWm^{-2}), and also in most of the SAC. From the four cross sections, we can observe the low temperatures and positive density anomalies (300–500°C and 50–60 kg/m^3), extending to the depths larger than 200 km beneath the WAC. Eastward, beneath the NAC, the upper mantle becomes moderately cold and dense (600–700°C and 30–40 kg/m^3) at intermediate depths (100–200 km), and warm and low dense (1000–1100°C and −20 kg/m^3) in the shallower part. The upper mantle sharply becomes significantly hotter (1000–1100°C), lower dense (−20 kg/m^3), and thinner (100–150 km) beneath the Phanerozoic terranes.

6.2. Final Thermal Model

The final thermal model is displayed for a depth of 100 km and along four cross sections in Figure 12. The estimated compositional variations lead to an increase of temperature by 100–150°C in the cratonic areas, with respect to the initial temperature, depending on the degree of depletion. The effect of the change in the attenuation model is minor, since the anelasticity has a significant effect only at temperatures exceeding ~900°C. On the other hand, in the interpretation of the negative density anomalies, the model does not take into account other low-density mineral phases, which may reduce the temperature, such as the amphibole.

Temperature increase is mainly observed in the WAC and NAC and causes a reduction of the temperature variations between the terranes of different ages and the consequent relocation of their lateral thermal boundaries, due to the shrinkage of the cold areas (Figure 12, cross sections A-A′, B-B′, C-C′, and D-D′). The increase of temperature clearly shows the thermal and thus viscosity contrasts between the cores of the WAC (Yilgarn and Pilbara cratons) and their margins.

Despite the temperature increase in the Archean and Proterozoic cratons, the sharp contrast with the relatively hot Phanerozoic upper mantle is retained. In Western Australia, the coolest temperatures in the upper

mantle (<800°C) deepens from ~100 km beneath the western margin (Pinjarra Orogen) to 220 km in the Yilgarn and Pilbara cratons and to 250 km beneath the Capricorn Orogen, following the observed thickening of the crust (Figure 12, cross sections A-A′ and B-B′). We would like to point out that this depth corresponds to the bottom limit of the coldest upper mantle layer, which does not necessarily coincide with the thermal lithosphere-asthenosphere boundary (LAB). The latter is quite elusive and can be traced as a depth of different isotherms (usually, between 1100°C and 1350°C), on account of the composition and physical conditions of the upper mantle (Cammarano et al., 2011). Therefore, the LAB detection is beyond the aim of this study, also considering that, according to the recent study of Fullea et al. (2020), in the WAC, the cratonic roots extend up to the top of the transition zone, then below the limit of our model.

Our model shows in the southern Canning Basin and in the central and southern part of the NAC high temperatures (1000–1100°C) in the uppermost mantle (down to a maximum depth of 120 km) and low temperatures (600–800°C) at larger depths. The shallow thermal anomaly of central Australia corresponds to elevated heat flow values (>80 mWm^{-2}), which have been interpreted as the product of anomalously high values of crustal heat production (McLaren et al., 2003). Since it is difficult to explain the existence of a hot shallow upper mantle in this region, considering its tectonic history, we suggest as in previous studies (e.g., Fishwick & Reading, 2008), a low-density mineral phase, such as amphibole, that may reduce the density relative to the initially assumed composition. The cold deep Archean lithospheric layer extends eastward beneath the shallow thermal anomaly, underlying terranes of Proterozoic age. The eastward extension of this cold deep lithospheric layer is sharply interrupted where it meets the hotter Phanerozoic upper mantle (cross sections A-A′, B-B′, C-C′, and D-D′). Southward, below the Officer and Eucla basins the cold upper mantle layer thickens, reaching a depth of ~220 km (Figure 12, cross section B-B′). Eastward of the Amadeus Basin, in the Euromanga Basin, the lower limit of the low-temperature upper mantle layer shallows to 150–160 km, (Figure 12, cross section C-C′). The SAC with Archean to Proterozoic surface exposures has a much thinner and warmer lithosphere than the other cratons.

We can observe that there is not a full agreement between the thermal anomalies observed in the uppermost mantle (~100 km) and those of the uppermost crust (Gerner & Holgate, 2010), as well as with the depths of magnetization estimated by Chopping and Kennett (2015). Indeed, the coldest crustal areas (<85°C) and large Curie depths (~ 70 km), correspond to the Archean WAC, which is characterized by a cold upper mantle as well. In contrast, the warmest crust (>235°C), enriched in heat producing elements, is observed in the Eromanga Basin, where the Curie depths is also very shallow (10 km) and the northern part of the NAC, but not in the easternmost part of the Australian Continent, underlain by a hot upper mantle. The reason of these discrepancies can be that in the crust, the temperature variations are strongly influenced by the distribution of the heat producing elements, while in the upper mantle, the temperature is directly influenced by tectonic processes, such as the extension, producing passive asthenosphere uprising, and plume activity. Therefore, the temperatures can show different patterns in the crust and upper mantle, depending on the origin of the thermal anomaly and diffusion time.

Finally, we want to point out that even if we cannot prove the reliability of the values of the thermal model, our results clearly evidence the temperature variations between the different continental regions and how sharp or gradual they occur.

6.3. Final Density Model and Compositional Variations in the Upper Mantle

We estimated the density variations in the upper mantle, by using the final thermal model, which takes into account the depletion and low attenuation of the upper mantle in the cratonic regions (Figure 11b). In comparison with the initial thermal-induced density variations (Figure 11a), the strong positive values in the cratonic areas are significantly reduced. In particular, looking at the cross sections, we can observe that the positive density anomaly beneath the WAC reaches the maximum depth at about 200 km (Figure 11b, cross sections A-A′, B-B′, and C-C′). In the Proterozoic terranes, the decrease, both in the amplitude and size, of the positive density anomalies relative to those induced by the initial thermal model at a depth of 100 km is accompanied by an increase of the amplitude and depth extension of the negative density anomalies localized in the uppermost mantle (<100 km) and a consequent reduction of the thickness of the high-density layer beneath them (Figure 11b, cross sections A-A′, C-C′, and D-D′). The significant reduction of the positive residual density values in the cratonic regions is due to the negative compositional anomalies (Figure 13a), obtained from the joint inversion of the residual mantle gravity anomalies and residual

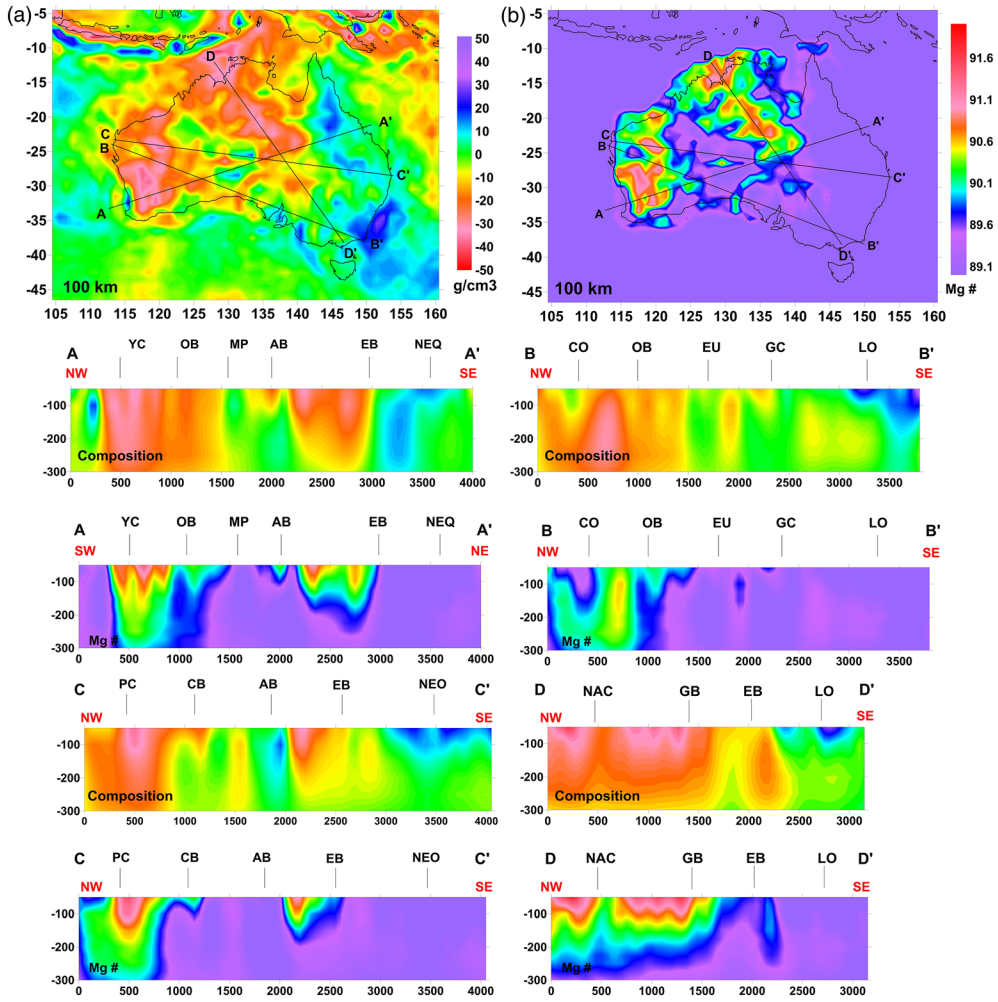

Figure 13. (a) Compoitional density variations and (b) *Fe* depletion variations in the Australian Continent in terms of Mg# (100 × Mg/(Mg + Fe)) in the Archean and Proterozoic upper mantle at a depth of 100 km and along four cross sections, estimated by fitting the negative compositional density anomalies in the cratonic areas. Black lines show the cross-sectional location and black labels, on the top of the cross sections, the abbreviations of the names of the main tectonic provinces displayed in Figure 1.

topography (section 5.4). As in Tesauro et al. (2014a), we estimated the iron depletion in terms of Mg# and percentage of mineral phases needed to explain the decrease of the positive final density variations in the cratonic area, with respect to the initial ones. The results shown in terms of Mg# variations at depths of 100 km and along four cross sections are displayed in Figure 13b. Since the resolution of the thermal model is limited to the resolution of seismic tomography, while that of the density model might be higher, we do not discuss the compositional anomalies, which are less in size than the thermal ones.

The largest negative compositional anomalies (~0.35 g/cm^3), corresponding to a Mg# 91–92, are located in the shallow part (<120 km) of the upper mantle beneath the Yilgarn and Pilbara cratons, while in the Capricorn Orogen, the depletion at the same depths is modest (~0.20 g/cm^3, Mg# ~ 90). The upper mantle of the WAC remains weakly depleted down to a depth of 300 km, indicating that it does not reach a fertile composition, even as temperatures increase in the lower part of the model (Figures 13a and 13b, cross sections A-A′, B-B′, and C-C′). Therefore, beneath the WAC, the depletion persists also below the cold upper mantle layer, indicating the presence of a thick layer of gradual transition from the lithosphere to asthenosphere, as already observed in previous seismic studies of Yoshizawa (2014) and Yoshizawa and Kennett (2015). In contrast, the upper mantle in the northern part of the NAC also is strongly depleted at shallow depths (down to 100 km), while below 200 km, the depletion becomes negligible (Mg# < 90).

The upper mantle of the central part of the Proterozoic terranes (Canning and Amadeus basins) and SAC is almost undepleted, despite the crystalline basement is Archean to Mesoproterozoic in age. Therefore, in these areas, the upper mantle has been either refertilized or potentially replaced, with a younger undepleted one.

7. Uncertainty Analysis

The initial data and methods used in this study suffer from several uncertatnties that are discussed in this section. First of all, we have to consider the uncertainties related to the crustal model (thickness and density of the layers composing the model). To this purpose, it is important to note that this analysis was applied not to a single point of the model but to relatively large-scale anomalies (at least, several hundred km wide), which have been obtained from a significant amount of seismic determinations. Mooney and Kaban (2010) analyzed in details such kind of uncertainties of the residual fields for North America. They concluded that the uncertainty related to the sedimentary cover could be about 10–12 mGal, 30–50 mGal for the Moho variations, and 25–50 mGal for the gravity effect of the crystalline crust, depending on the seismic data coverage. The uncertainty related to the crystalline crust was estimated taking into account the velocity-to-density conversion. Since, in this case, errors of the velocity structure models are not specified, this estimation represents a lower limit. On the other hand, previous gravity-based studies targeting the Moho and crustal density (Aitken et al., 2013) and the lithospheric density field (Aitken et al., 2015) included comprehensive sensitivity analyses. These models provide an indication of the likely effect of errors in AuSREM on the final results. For the Moho modeling (Aitken et al., 2013), variability in results is typically within ±3 km (2 s), while at the lithospheric scale (Aitken et al., 2015), the range in crustal density variation is typically <30 kg/m^3. In terms of net crustal gravity effect, these uncertainties are of the order of ±50 mGal, thus in the same range of those calculated by Mooney and Kaban (2010). Furthermore, possible input of different factors may be considered as independent, and thus, the total impact of their uncertainty should be significantly reduced. Correspondingly, for large-scale anomalies, calculated on the base on ten to hundred crustal probings, which are available in Australia, due to dense seismic networks, uncertainties may reach 30–50 mGal and 0.3–0.4 km for the residual gravity and topography, respectively, depending on the crustal thickness (larger for the thick crust; Mooney & Kaban, 2010). The related uncertainties translated to mantle density variation depend on thickness of the layer, to which they are applied. For the 100-km-thick layer, they approximately correspond to 10 kg/m^3. Therefore, most of the calculated mantle gravity anomalies are reliable, since their amplitudes exceed the error threshold. Furthermore, in the inversion scheme, we kept the shallow layer related to the crust, which can accommodate the effect of additional density anomalies (section 5.4).

The uncertainties of the thermal model are mainly depending on those of the seismic topography models, which are difficult to quantify, due to their dependency on several factors (e.g., crustal and seismic reference model used, inhomogeneous ray coverage, regularization schemes; Foulger et al., 2013). In particular, the AuSREM seismic tomography models were released without quantification of their uncertainties, as usual in most seismic studies. However, we should consider that rather broad seismic anomalies (several hundred km wide), which are usually covered by a large amount of data, are well constrained. Therefore, as for the crustal model, we did not consider the reliability of a single point but of broad areas with good ray coverage. For these reasons, it is hard to quantify the uncertainty of the thermal model related to the seismic tomography model. However, to get an idea about the effect of the uncertainty produced by a seismic tomography model on temperature and consequently on density, we should consider that an absolute velocity variation of 0.3% corresponds to a temperature variation of 100°C (even less for temperature greater than 900°C, due to the anelasticity effect, which makes the velocity-temperature conversion nonlinear) and a density deviation of about 10 kg/m^3. Other uncertainties of the thermal model are related to those of the elastic parameters, which are considered small (Cammarano et al., 2003), and the anelasticity that has not a significant effect in the cratonic areas (section 5.3). Indeed, the difference in temperature produced by two end-member models of anelasticity (representative of a “dry” and “wet” upper mantle, respectively) is negligible at low temperatures (<900°C) and becomes significant only close to the melting point (~200°C). Therefore, also the main uncertainty of the estimated depletion depends on those of the seismic velocity model. To this purpose, we should note that a variation in depletion of 1.0 unit in Mg# and corresponding fractions of the mineral

phases corresponds to a density change of 16 kg/m^3 (section 6.3), which is a greater value than that produced by an uncertainty of 0.3% in seismic velocity.

8. Discussion

Even if the input parameters of the thermal and compositional model are affected by some uncertainties (discussed in section 7), the obtained results help us understand the present day lithospheric properties and past tectonic evolution of the Australian Continent. The results show similar patterns to some previous studies of the Australia's lithosphere, which clearly identify the sharp transition between the Precambrian and the Phanerozoic terranes and the low-velocity anomaly in central Australia (Aitken et al., 2015; Fichtner et al., 2005, 2010; Fishwick & Rawlinson, 2012; Fishwick & Reading, 2008; Goes et al., 2005; Kennett & Salmon, 2012; Rawlinson & Fishwick, 2012; Yoshizawa, 2014; Yoshizawa & Kennett, 2015), but provide important additional details on the temperatures distribution among the different cratonic blocks and a clearer discrimination of thermal and compositional influences. Our model shows also substantial differences with other previous results. For instance, we observe that the coldest part of the upper mantle (<800°C) reaches the maximum depth (~200 km) beneath the WAC, while the model of Khan et al. (2013) shows a progressive increase of temperature with depth, with the deepest lithospheric roots (~250 km) localized in correspondence of the NAC.

According to previous studies using xenolith data (e.g., Gaul et al., 2003), the compositional layering that we observed in the Precambrian Australian cratons is the result of a moderate-high-depleted uppermost mantle and then a metasomatically refertilized lower part, as an effect of the addition of *Fe*-rich material through an increasing degree of melt-related metasomatism with depth. Alternatively, the layering could also reflect an increasing degree of partial melt extraction at shallower depths during large-scale melting events. In Archean cratons, a multilayered lithosphere may also represent a compositionally buoyant core, with a lower layer of thermally stabilized lithosphere (Yuan & Romanowicz, 2010). Finally, during major tectonic events, such as mantle plume and delamination, the lithosphere may be almost entirely replaced with a younger and less depleted lithosphere (Gao et al., 2002; Xu, 2001).

The WAC has by far the best preserved Archean geology among the Australian cratons, and the lithospheric structure imaged here is consistent with that, including a >200-km-thick lithosphere characterized by low-temperature and a depleted composition (Mg# > 90.5). In our model, the Capricorn Orogen lithosphere is distinct, with similar temperature, but higher density associated with a less depleted composition. This may, in part, represent the younger Glenburgh Terrane (2,550–2,450 Ma), the formation of a Proterozoic lithosphere during the collisional events, and subsequent intraplate reworking (Johnson et al., 2011). Differently than in previous studies (Fishwick et al., 2005; Fishwick & Rawlinson, 2012; Fishwick & Reading, 2008), we also observe that the cold lithospheric layer shows similar thickness and density beneath the Yilgarn and Pilbara cratons, likely indicating a commonality of processes of lithospheric formation. Furthermore, the southernmost edge of the Yilgarn Craton is characterized by a thin fertile lithosphere, which can be the result of the fluids metasomatization acted along its side, during the accretion of the surrounding orogenic belts.

In our model, the NAC is characterized by moderate temperatures and densities, with a lithosphere extending to ~200-km deph. Compositionally, the NAC lithosphere is depleted, although not so strongly as the WAC, with Mg# around 90.5. This confirms the presence of an Archean lithosphere beneath the northern NAC, but perhaps a younger lithosphere than in the WAC, or with a larger degree of modification during the subsequent Proterozoic events that widely affected the region (e.g., formation and fragmentation of the Centralian Superbasin).

The geological similarity of the SAC and the NAC suggests that these may have been contiguous, at least until the late Paleoproterozoic, before plate-scale reorganization occurred in the early Mesoproterozoic (Aitken et al., 2016; Betts et al., 2016; Giles et al., 2004). This reorganization was associated with intense reworking of the Gawler and Curnamona regions, including oroclinal bending, arc-like magmatism and the Hiltaba magmatic event, perhaps plume associated (Betts et al., 2009, 2016). Furthermore, the late Neoproterozoic Delamerian Orogeny has had a pervasive influence on the SAC (Hand et al., 2007; Williams & Betts, 2009). Our model suggests quite a different lithospheric structure of the SAC with respect to the NAC, being dominated by high temperatures, moderate density, and an undepleted composition

(Mg# < 89.5). This is consistent with the replacement or refertilization of the lithosphere as part of the younger tectonic events that affected this region, but not the NAC.

The boundaries between these three cratons are defined by Proterozoic orogens that are found in central Australia, roughly in a Y-geometry (Myers et al., 1996). These orogens record crustal growth during the Paleoproterozoic to Mesoproterozoic, with new crust forming as late as ~1.4 Ga (Spaggiari et al., 2018). Subsequently, the lithosphere was subjected to several intense events, including prolonged ultrahigh-temperature orogenesis (Smithies et al., 2011) and several LIP events (Glass & Phillips, 2006; Wingate et al., 2004; Zhao et al., 1994). These events have had a profound effect on lithospheric structure, including potentially the formation of a slow-velocity layer in the uppermost mantle (Fichtner et al., 2010; Fishwick & Reading, 2008) and a similarly located magmatic underplate (Alghamdi et al., 2018). In our model, these orogens show variable lithospheric temperature and density, in a lithosphere up to 250 km thick. Cool, high-density lithosphere exists in the southwestern part (Albany-Fraser Orogen), with somewhat warmer and less dense lithosphere to the north, northwest, and east, perhaps associated with increasing crustal heat production. Composition in this "Y" zone is consistently undepleted (Mg# < 89.5), except for some smaller areas that may possess residual crustal effects. This is consistent with a Proterozoic lithosphere throughout this region.

The Tasmanides developed partly on a Proterozoic continental lithosphere but also younger oceanic lithosphere, with a "stepped" lithosphere from ~140°E to 145°E (Fishwick et al., 2008). Our model shows a centrally located region with lower temperatures and higher density defining a lithosphere between 150 and 200 km thick. This is surrounded by much warmer and less dense mantle with a sharp to gradational transition. Composition is undepleted throughout Eastern Australia (Mg# < 89.5).

Finally, the eastern and southeastern fringe of the continent is defined by high to very high temperatures and higher density mantle than seen elsewhere. The greatest temperatures and lowest densities are seen in northeast Queensland, and beneath Bass Strait, Tasmania, and southern Victoria. These regions were all reactivated during Mesozoic breakup of Gondwana, with variable amounts of uplift, extension, and magmatism associated with this process. Northeast Queensland and southern Victoria also possess recent volcanism (Rawlinson et al., 2017). At the broadest scale, this feature is interpreted to represent the thermal perturbation of the mantle associated with these Mesozoic and Cenozoic events.

9. Conclusions

This study aims at improving our understanding of the Australia's lithosphere and its evolution through modeling of its thermal and compositional structure. The key results comprise determination of structure and properties of the upper mantle layers, which vary in different regions. These results improve our knowledge about formation and evolution of Australian lithosphere.

The Archean WAC and Archean-Paleoproterozoic NAC are characterized by the thick and relatively cold, upper mantle that has a depleted composition (Mg# > 90). We suggest that this characteristic depletion indicates the degree of preservation of the Archean upper mantle. Although geologically similar to the NAC, the SAC is characterized by a much less depleted upper mantle, and we suggest that this is the result of refertilization occurred during the Proterozoic tectonic events.

The Proterozoic lithosphere is preserved in central Australia and in the central part of Eastern Australia, which is characterized by a weakly depleted or undepleted composition, with variable density and thicknesses of the cold part of the mantle lithosphere (<1000°C) between 150 and 200 km. Finally, substantially hotter and less dense lithosphere is seen fringing the eastern and southeastern margin of the continent, indicating the presence of a thin lithosphere in these regions in response to the Mesozoic and Cenozoic tectonic events.

Data Availability Statement

The figure displaying the gravity effect and residual topography induced by composition is shown in Figure S1. The 3D thermal model, density model of the crust, and residual density of the upper mantle (adjusted density model) are available in the public domain repository, National Geoscience Data Centre (http://www.bgs.ac.uk/services/ngdc/).

Acknowledgments

This study was funded by Trieste University (FABBR-2018), Utrecht University, the Netherlands Research Centre for Integrated Solid Earth Science (ISES-2016-UU-19), DFG (German Research Foundation), SPP-1788 Dynamic Earth (KA2669/4-1, KA2669/4-2, and KA2669/6-1). The comments of J.-C. Afonso, W. Levandowski, and three anonymous reviewers on an earlier version have greatly improved the manuscript.

References

Aitken, A. R. A., Altinay, C., & Gross, L. (2015). Australia's lithospheric density field and its isostatic equilibration. *Geophysical Journal International*, *203*(3), 1961–1976. https://doi.org/10.1093/gji/ggv396

Aitken, A. R. A., Betts, P. G., Young, D. A., Blankenship, D. D., Roberts, J. L., & Siegert, M. J. (2016). The Australo-Antarctic Columbia to Gondwana transition. *Gondwana Research*, *29*, 136–152.

Aitken, A. R. A., Salmon, M. L., & Kennett, B. L. N. (2013). Australia's Moho: A test of the usefulness of gravity modelling for the determination of Moho depth. *Tectonophysics*, *609*, 468–479. https://doi.org/10.1016/j.tecto.2012.06.049

Alghamdi, A. H., Aitken, A. R. A., & Dentith, M. C. (2018). The deep crustal structure of the Warakurna LIP, and insights on Proterozoic LIP processes and mineralisation. *Gondwana Research*, *56*, 1–11. https://doi.org/10.1016/j.gr.2017.12.001

Betts, P. G., Armit, R. J., Stewart, J., Aitken, A. R. A., Ailleres, L., Donchak, P., et al. (2016). Australia and Nuna. *Geological Society Special Publication*, *424*(1), 47–81. https://doi.org/10.1144/SP424.2

Betts, P. G., Giles, D., Foden, J., Schaefer, B. F., Mark, G., Pankhurst, M. J., et al. (2009). Mesoproterozoic plume-modified orogenesis in eastern Precambrian Australia. *Tectonics*, *28*, TC3006. https://doi.org/10.1029/2008TC002325

Betts, P. G., Giles, D., Lister, G. S., & Frick, L. R. (2002). Evolution of the Australian lithosphere. *Australian Journal of Earth Sciences*, *49*(4), 661–695. https://doi.org/10.1046/j.1440-0952.2002.00948.x

Brenhin Keller, C., & Schoene, B. (2012). Statistical geochemistry reveals disruption in secular lithospheric evolution about 2.5 Gyr ago. *Nature*, *485*(7399), 490–493. https://doi.org/10.1038/nature11024

Brown, M. (2007). Metamorphic conditions in orogenic belts: A record of secular change. *International Geology Review*, *49*(3), 193–234. https://doi.org/10.2747/0020-6814.49.3.193

Cammarano, F., Goes, S., Vacher, P., & Giardini, D. (2003). Inferring upper-mantle temperatures from seismic velocities. *Physics of the Earth and Planetary Interior*, *138*(3–4), 197–222. https://doi.org/10.1016/S00319201(03)00156-0

Cammarano, F., Tackley, P., & Boschi, L. (2011). Seismic, petrological and geodynamical constraints on thermal and compositional structure of the upper mantle: Global thermochemical models. *Geophysics Journal International*, *187*, 1301–1318.

Cawood, P. A. (2005). Terra Australis Orogen: Rodinia breakup and development of the Pacific and Iapetus margins of Gondwana during the Neoproterozoic and Paleozoic. *Earth-Science Reviews*, *69*(3–4), 249–279. https://doi.org/10.1016/j.earscirev.2004.09.001

Cawood, P. A., & Korsch, R. J. (2008). Assembling Australia: Proterozoic building of a continent. *Precambrian Research*, *166*(1–4), 1–35. https://doi.org/10.1016/j.precamres.2008.08.006

Chevrot, S., & van der Hilst, R. D. (2000). The Poisson ratio of the Australian crust: Geological and geophysical implications. *Earth and Planetary Science Letters*, *183*(1–2), 121–132. https://doi.org/10.1016/S0012-821X(00)00264-8

Chopping, R., & Kennett, B. L. N. (2015). Maximum depth of magnetisation of Australia, its uncertainty, and implications for curie depth. *GeoResJ*, *7*, 70–77. https://doi.org/10.1016/j.grj.2015.06.003

Christensen, N. I., & Mooney, W. D. (1995). Seismic velocity structure and composition of the continental crust: A global review. *Journal Geophysical Research*, *100*(B6), 9761–9788.

Clitheroe, G., Gudmundsson, O., & Kennett, B. L. N. (2000). The crustal thickness of Australia. *Journal Geophysical Research*, *105*(B6), 13,697–13,713. https://doi.org/10.1029/1999JB900317

Condie, K. C. (2004). Supercontinents and superplume events: Distinguishing signals in the geologic record. *Physics of the Earth and Planetary Interiors*, *146*(1–2), 319–332. https://doi.org/10.1016/j.pepi.2003.04.002

Direen, N. G., & Crawford, A. J. (2003). The Tasman line: Where is it, and is it Australia's Rodinian breakup boundary? *Australian Journal of Earth Science*, *50*(4), 491–502. https://doi.org/10.1046/j.1440-0952.2003.01005.x

Fichtner, A., Kennett, B. L. N., Igel, H., & Bunge, H. P. (2010). Full waveform tomography for radially anisotropic structure: New insights into present and past states of the Australasian upper mantle. *Earth and Planetary Science Letters*, *290*(3–4), 270–280. https://doi.org/10.1016/j.epsl.2009.12.003

Fishwick, S., Heintz, M., Kennett, B. L. N., Reading, A. M., & Yoshizawa, K. (2008). Steps in lithospheric thickness within Eastern Australia, evidence from surface wave tomography. *Tectonics*, *27*, TC4009. https://doi.org/10.1029/2007TC002116

Fishwick, S., Kennett, B. L. N., & Reading, A. M. (2005). Contrasts in lithospheric structure within the Australian craton—Insights from surface wave tomography. *Earth and Planetary Science Letters*, *231*(3–4), 163–176. https://doi.org/10.1016/j.epsl.2005.01.009

Fishwick, S., & Rawlinson, N. (2012). 3-D structure of the Australian lithosphere from evolving seismic datasets. *Australian Journal of Earth Sciences: An International Geoscience Journal of the Geological Society of Australia*, *59*(6), 809–826. https://doi.org/10.1080/08120099.2012.702319

Fishwick, S., & Reading, A. M. (2008). Anomalous lithosphere beneath the Proterozoic of western and central Australia: A record of continental collision and intraplate deformation? *Precambrian Research*, *166*, 111–121.

Fontaine, F. R., Tkalčić, H., & Kennett, B. L. N. (2013). Imaging crustal structure variation across southeastern Australia. *Tectonophysics*, *582*, 112–125. https://doi.org/10.1016/j.tecto.2012.09.031

Förste, C., Bruinsma, S. L., Abrikosov, O., Lemoine, J.-M., Marty, J. C., Flechtner, F., et al. (2014). EIGEN-6C4: The latest combined global gravity field model including GOCE data up to degree and order 2190 of GFZ Potsdam and GRGS Toulouse. *GFZ Data Services.* http://doi.org/10.5880/icgem.2015.1

Foulger, G. R., Panza, G. F., Artemieva, I. M., Bastow, I. D., Cammarano, F., Evans, J. R., et al. (2013). Caveats on tomographic images. *Terra Nova*, *25*(4), 259–281. https://doi.org/10.1111/ter.12041

Fullea, J., Lebedev, S., Martinec, Z., & Celli, N. L. (2020). Unravelling the upper mantle heterogeneity from integrated multi-observable inversions. *EGU Presentation*, 2020–2685.

Gao, S., Rudnick, R. L., Carlson, R. W., McDonough, W. F., & Liu, Y. S. (2002). Re-Os evidence for replacement of ancient mantle lithosphere beneath the north China craton. *Earth and Planetary Science Letters*, *198*(3–4), 307–322. https://doi.org/10.1016/S0012-821X(02)00489-2

Gardner, G. H. F., Gardner, L. W., & Gregory, A. R. (1974). Formation velocity and density—The diagnostic basics for stratigraphic traps. *Geophysics*, *39*(6), 770–780. https://doi.org/10.1190/1.1440465

Gaul, O. F., O'Reilly, S. Y., & Griffin, W. L. (2003). Lithosphere structure and evolution in southeastern Australia. *Special Paper of the Geological Society of America*, *372*, 185–202.

Gerner, E., & Holgate, F. (2010). Oztemp interpreted temperature at 5 km depth. Canberra: Digital data. Geoscience Australia. GEOCAT reference, 71143.

Giles, D., Betts, P. G., & Lister, G. S. (2004). 1.8-1.5 Ga links between the North and South Australian cratons and the early-middle Proterozoic configuration of Australia. *Tectonophysics*, *380*(1–2), 27–41. https://doi.org/10.1016/j.tecto.2003.11.010

Glass, L. M., & Phillips, D. (2006). The Kalkarindji continental flood basalt province: A new Cambrian large igneous province in Australia with possible links to faunal extinctions. *Geology*, *34*(6), 461–464. https://doi.org/10.1130/G22122.1

Glen, R. A. (2005). The Tasmanides of Eastern Australia. *Geological Society Special Publication*, *246*(1), 23–96. https://doi.org/10.1144/GSL.SP.2005.246.01.02

Goes, S., Simons, F. J., & Yoshizawa, K. (2005). Seismic constraints on temperature of the Australian uppermost mantle. *Earth and Planetary Science Letters*, *236*(1–2), 227–237. https://doi.org/10.1016/j.epsl.2005.05.001

Griffin, W. L., O'Reilly, S. Y., Abe, N., Aulback, S., Davies, R. M., Pearson, N. J., et al. (2003). The origin and evolution of Archean lithospheric mantle. *Precambrian Research*, *127*(1–3), 19–41. https://doi.org/10.1016/S0301-9268(03)00180-3

Griffin, W. L., O'Reilly, S. Y., Afonso, J. C., & Begg, G. C. (2009). The composition and evolution of lithospheric mantle: A re-evaluation and its tectonic implications. *Journal of Petrology*, *50*(7), 1185–1204. https://doi.org/10.1093/petrology/egn033

Groves, D. I., Condie, K. C., Goldfarb, R. J., Hronsky, J. M. A., & Vielreicher, R. M. (2005). 100th anniversary special paper: Secular changes in global tectonic processes and their influence on the temporal distribution of gold-bearing mineral deposits. *Economic Geology*, *100*(2), 203–224. https://doi.org/10.2113/gsecongeo.100.2.203

Haeger, C., Kaban, M. K., Tesauro, M., Petrunin, A. G., & Mooney, W. D. (2019). 3D density, thermal and compositional model of the Antarctic lithosphere and implications for its evolution. *Geochemistry, Geophysics, Geosystems*, *20*, 688–707. https://doi.org/10.1029/2018GC008033

Hand, M., Reid, A., & Jagodzinski, L. (2007). Tectonic framework and evolution of the Gawler craton, Southern Australia. *Economic Geology*, *102*(8), 1377–1395. https://doi.org/10.2113/gsecongeo.102.8.1377

Hoggard, M. J., Czarnota, K., Richards, F. D., Huston, D. L., Jaques, A. L., & Ghelichkhan, S. (2020). Global distribution of sediment-hosted metals controlled by craton edge stability. *Nature Geoscience*, *13*(7), 504–510. https://doi.org/10.1038/s41561-020-0593-2

Hollis, J. A., Kirkland, C. L., Spaggiari, C. V., Tyler, I. M., Haines, P. W., Wingate, M. T. D., et al. (2013). Zircon U–Pb–Hf isotope evidence for links between the Warumpi and Aileron provinces, west Arunta region. *Geological Survey of Western Australia, Record 2013/9*, 30.

Johnson, S. P., Sheppard, S., Rasmussen, B., Wingate, M. T. D., Kirkland, C. L., Muhling, J. R., et al. (2011). Two collisions, two sutures: Punctuated pre-1950Ma assembly of the West Australian Craton during the Ophthalmian and Glenburgh Orogenies. *Precambrian Research*, *189*(3–4), 239–262. https://doi.org/10.1016/j.precamres.2011.07.011

Kaban, M. K., El Khrepy, S., & Al-Arifi, N. (2016). Isostatic model and isostatic gravity anomalies of the Arabian plate and surroundings. *Pure and Applied Geophysics*, *173*(4), 1211–1221. https://doi.org/10.1007/s00024-015-1164-0

Kaban, M. K., Mooney, W. D., & Petrunin, A. G. (2015). Cratonic root beneath North America shifted by basal drag from the convecting mantle. *Nature Geoscience*, *8*(10), 797–800. https://doi.org/10.1038/ngeo2525

Kaban, M. K., Petrunin, A. G., Schmeling, H., & Shahraki, M. (2014). the observed geoid. *Surveys in Geophysics*, *35*(6), 1361–1373. https://doi.org/10.1007/s10712-014-9281-3

Kaban, M. K., Schwintzer, P., Artemieva, I. M., & Mooney, W. D. (2003). Density of the continental roots: Compositional and thermal contributions. *Earth and Planetary Science Letters*, *209*(1–2), 53–69. https://doi.org/10.1016/S0012-821X(03)00072-4

Kaban, M. K., Schwintzer, P., & Reigber, C. (2004). A new isostatic model of the lithosphere and gravity field. *Journal of Geodesy*, *78*(6), 368–385. https://doi.org/10.1007/s00190-004-0401-6

Kaban, M. K., Stolk, W., Tesauro, M., El Khrepy, S., Al-Arifi, N., Beekman, F., & Cloetingh, S. A. P. L. (2016). 3D density model of the upper mantle of Asia based on inversion of gravity and seismic tomography data. *Geochemistry, Geophysics, Geosystems*, *17*, 4457–4477. https://doi.org/10.1002/2016GC006458

Kaban, M. K., Tesauro, M., & Cloetingh, S. (2010). An integrated gravity model for Europe's crust and upper mantle. *Earth and Planetary Science Letters*, *296*(3–4), 195–209. https://doi.org/10.1016/j.epsl.2010.04.041

Kaban, M. K., Tesauro, M., Mooney, W. D., & Cloetingh, S. A. P. L. (2014). Density, temperature, and composition of the North American lithosphere—New insights from a joint analysis of seismic, gravity, and mineral physics data: 1. Density structure of the crust and upper mantle. *Geochemistry, Geophysics, Geosystems*, *15*, 4781–4807. https://doi.org/10.1002/2014GC005483

Kennett, B. L. N., Fichtner, A., Fishwick, S., & Yoshizawa, K. (2013). Australian seismological referencemodel (AuSREM): Mantle component. *Geophysical Journal International*, *192*(2), 871–887. https://doi.org/10.1093/gji/ggs065

Kennett, B. L. N., Fishwick, S., Reading, A. M., & Rawlinson, N. (2004). Contrasts in mantle structure beneath Australia: Relation to Tasman lines? *Australian Journal of Earth Sciences*, *51*(4), 563–569. https://doi.org/10.1111/j.1400-0952.2004.01075.x

Kennett, B. L. N., & Salmon, M. (2012). AuSREM: Australian Seismological Reference Model. *Australian Journal of Earth Sciences*, *59*(8), 1091–1103. https://doi.org/10.1080/08120099.2012.736406

Kennett, B. L. N., Yoshizawa, K., & Furumurac, T. (2017). Interactions of multi-scale heterogeneity in the lithosphere: Australia. *Tectonophysics*, *717*, 193–213. https://doi.org/10.1016/j.tecto.2017.07.009

Khan, A., Zunino, A., & Deschamps, F. (2013). Upper mantle compositional variations and discontinuity topography imaged beneath Australia from Bayesian inversion of surface-wave phase velocities and thermochemical modeling. *Journal of Geophysical Research: Solid Earth*, *118*, 5285–5306. https://doi.org/10.1002/jgrb.50304

Kirkland, C. L., Johnson, S. P., Smithies, R. H., Hollis, J. A., Wingate, M. T. D., Tyler, I. M., et al. (2013). Not-so-suspect terrane: Constraints on the crustal evolution of the Rudall Province. *Precambrian Research*, *235*, 131–149. https://doi.org/10.1016/j.precamres.2013.06.002

Kirkland, C. L., Spaggiari, C. V., Pawley, M. J., Wingate, M. T. D., Smithies, R. H., Howard, H. M., et al. (2011). On the edge: U-Pb, Lu-Hf, and Sm-Nd data suggests reworking of the Yilgarn Craton margin during formation of the Albany-Fraser Orogen. *Precambrian Research*, *187*, 223–247.

Laske, G., Masters, G., Ma, Z., & Pasyanos, M. (2013). Update on CRUST1.0—A 1-degree global model of Earth's crust. In *EGU General Assembly 2013* (Vol. 15, p. 2658). Retrieved from https://ui.adsabs.harvard.edu/abs/2013EGUGA..15.2658L/abstract

McDonough, W. F., & Sun, S.-S. (1995). The composition of the earth. *Chemical Geology*, *120*, 223–253.

McLaren, S., Sandiford, M., Hand, M., Neumann, N., Wyborn, L., & Bastrakova, I. (2003). The hot southern continent: Heat flow and heat production in Australian Proterozoic terranes. In: R. R. Hillis & R. D. Müller (Eds.), *Evolution and dynamics of the Australian Plate*. Geol. Soc. Am. Spec. Pap. 372. *Geol. Soc. Aus. Spec. Pub*, 22.

Mooney, W. D., & Kaban, M. K. (2010). The North American upper mantle: Density, composition, and evolution. *Journal of Geophysical Research*, *115*, B12424. https://doi.org/10.1029/2010JB000866

Murphy, J. B., & Nance, R. D. (2012). Speculations on the mechanisms for the formation and breakup of supercontinents. *Geoscience Frontiers*, *4*(2), 185–194.

Myers, J. S., Shaw, R. D., & Tyler, I. M. (1996). Tectonic evolution of Proterozoic Australia. *Tectonics*, *15*(6), 1431–1446. https://doi.org/10.1029/96TC02356

Nance, R. D., Murphy, J. B., & Santosh, M. (2014). The supercontinent cycle: A retrospective essay. *Gondwana Research*, *25*(1), 4–29. https://doi.org/10.1016/j.gr.2012.12.026

Nolet, G. (1990). Partitioned waveform inversion and two-dimensional structure under the network of autonomously recording seismograph. *Journal of Geophysical Research*, *95*(B6), 8499–8512. https://doi.org/10.1029/JB095iB06p08499

O'Really, S. Y., Griffin, W. L., & Gaul, O. (1997). Paleogeothermal gradients in Australia: Key to 4-D lithosphere mapping. *AGSO Journal of Australian Geology & Geophysics*, *17*(1), 63–72.

Rawlinson, N., Davies, D. R., & Pilia, S. (2017). The mechanisms underpinning Cenozoic intraplate volcanism in Eastern Australia: Insights from seismic tomography and geodynamic modeling. *Geophysical Research Letters*, *44*, 9681–9690. https://doi.org/10.1002/2017GL074911

Rawlinson, N., & Fishwick, S. (2012). Seismic structure of the southeast Australian lithosphere from surface and body wave tomography. *Tectonophysics*, *572–573*, 111–122.

Rawlinson, N., Salmon, M., & Kennett, B. L. N. (2014). Transportable seismic array tomography in southeast Australia: Illuminating the transition from Proterozoic to Phanerozoic lithosphere. *Lithos*, *189*, 65–76. https://doi.org/10.1016/j.lithos.2013.06.001

Reddy, S. M., & Evans, D. A. D. (2009). Palaeoproterozoic supercontinents and global evolution: Correlations from core to atmosphere. *Geological Society Special Publication*, 1–26.

Ritsema, J., Deuss, A., van Heijst, H. J., & Woodhouse, J. H. (2011). S40RTS: A degree-40 shear velocity model for the mantle from new Rayleigh wave dispersion, teleseismic raveltime and normal-mode splitting function measurement. *Geophysical Journal International*, *184*(3), 1223–1236. https://doi.org/10.1111/j.1365-246X.2010.04884.x

Rogers, J. J. W., & Santosh, M. (2003). Supercontinents in earth history. *Gondwana Research*, *6*(3), 357–368. https://doi.org/10.1016/S1342-937X(05)70993-X

Root, B. C. (2020). Comparing global tomography-derived and gravity-based upper mantle density models. *Geophysical Journal International*, *221*(3), 1542–1554. https://doi.org/10.1093/gji/ggaa091

Rosenbaum, G. (2018). The Tasmanides: Phanerozoic tectonic evolution of Eastern Australia. *Annual Review of Earth and Planetary Sciences*, *46*(1), 291–325. https://doi.org/10.1146/annurev-earth-082517-010146

Salmon, M., Kennett, B. L. N., & Saygin, E. (2013). Australian seismological reference model (AuSREM): Crustal component. *Geophysical Journal International*, *192*, 190–206.

Santosh, M., Maruyama, S., & Yamamoto, S. (2009). The making and breaking of supercontinents: Some speculations based on superplumes, super downwelling and the role of tectosphere. *Gondwana Research*, *15*(3–4), 324–341. https://doi.org/10.1016/j.gr.2008.11.004

Schaeffer, A. J., & Lebedev, S. (2013). Global shear-speed structure of the upper mantle and transition zone. *Geophysical Journal International*, *194*(1), 417–449.

Smithies, R. H., Howard, H. M., Evins, P. M., Kirkland, C. L., Kelsey, D. E., Hand, M., et al. (2011). High-temperature granite magmatism, crust-mantle interaction and the mesoproterozoic intracontinental evolution of the Musgrave Province, central Australia. *Journal of Petrology*, *52*(5), 931–958. https://doi.org/10.1093/petrology/egr010

Spaggiari, C. V., Smithies, R. H., Kirkland, C. L., Wingate, M. T. D., England, R. N., & Lu, Y. J. (2018). Buried but preserved: The Proterozoic Arubiddy Ophiolite, Madura Province, Western Australia. *Precambrian Research*, *317*, 137–158. https://doi.org/10.1016/j.precamres.2018.08.025

Steinberger, B., & Calderwood, A. R. (2006). Models of large-scale viscous flow in the Earth's mantle with constraints from mineral physics and surface observations. *Geophysical Journal International*, *167*(3), 1461–1481. https://doi.org/10.1111/j.1365-246X.2006.03131.x

Stixrude, L., & Lithgow-Bertelloni, C. (2005). Thermodynamics of mantle minerals—I. Physical properties. *Geophysical Journal International*, *162*(2), 610–632. https://doi.org/10.1111/j.1365-246X.2005.02642.x

Stolk, W., Kaban, M. K., Beekman, F., Tesauro, M., Mooney, W. D., & Cloetingh, S. (2013). High resolution regional crustal models from irregularly distributed data: Application to Asia and adjacent areas. *Tectonophysics*, *602*, 55–68. https://doi.org/10.1016/j.tecto.2013.01.022

Tesauro, M., Kaban, M. K., & Cloetingh, S. A. P. L. (2008). EuCRUST-07: A new reference model for the European crust. *Geophysical Research Letters*, *35*, L05313.

Tesauro, M., Kaban, M. K., Mooney, W. D., & Cloetingh, S. A. P. L. (2014a). Density, temperature, and composition of the North American lithosphere—New insights from a joint analysis of seismic, gravity, and mineral physics data: 2. Thermal and compositional model of the upper mantle. *Geochemistry, Geophysics, Geosystems*, *15*, 4808–4830. https://doi.org/10.1002/2014GC005484

Tesauro, M., Kaban, M. K., Mooney, W. D., & Cloetingh, S. A. P. L. (2014b). A 3D model for the crustal structure of the North American Continent. *Tectonophysics*, *631*, 65–86. https://doi.org/10.1016/j.tecto.2014.04.016

Van Kranendonk, M. J., & Kirkland, C. L. (2016). Conditioned duality of the Earth system: Geochemical tracing of the supercontinent cycle through Earth history. *Earth-Science Reviews*, *160*, 171–187. https://doi.org/10.1016/j.earscirev.2016.05.009

Visser, K., Trampert, J., & Kennett, B. L. N. (2008). Global anisotropic phase-velocity maps for higher mode love and Rayleigh waves. *Geophysical Journal International*, *172*(3), 1016–1032. https://doi.org/10.1111/j.1365-246X.2007.03685.x

Walter, M. R., Veevers, J. J., Calver, C. R., & Grey, K. (1995). Neoproterozoic stratigraphy of the Centralian Superbasin, Australia. *Precambrian Research*, *73*, 173–195.

Williams, H. A., & Betts, P. G. (2009). The Benagerie Shear Zone: 1100 Myr of reactivation history and control over continental lithospheric deformation. *Gondwana Research*, *15*(1), 1–13. https://doi.org/10.1016/j.gr.2008.06.006

Wingate, M. T. D., Pirajno, F., & Morris, P. A. (2004). Warakurna large igneous province: A new Mesoproterozoic large igneous province in west-central Australia. *Geology*, *32*(2), 105–108. https://doi.org/10.1130/G20171.1

Xu, Y. G. (2001). Thermo-tectonic destruction of the archaean lithospheric keel beneath the Sino-Korean Craton in China: Evidence, timing and mechanism. *Physics and Chemistry of the Earth, Part A: Solid Earth and Geodesy*, *26*(9–10), 747–757. https://doi.org/10.1016/S1464-1895(01)00124-7

Yoshizawa, K. (2014). Radially anisotropic 3-D shear wave structure of the Australian lithosphere and asthenosphere from multi-mode surface waves. *Physics of the Earth and Planetary Interiors*, *235*, 33–48. https://doi.org/10.1016/j.pepi.2014.07.008

Yoshizawa, K., & Kennett, B. (2015). The lithosphere-asthenosphere transition and radial anisotropy beneath the Australian Continent. *Geophysical Research Letters*, *42*, 3839–3846. https://doi.org/10.1002/2015GL063845

Yuan, H. (2015). Secular change in Archaean crust formation recorded in Western Australia. *Nature Geoscience*, *8*(10), 808–813. https://doi.org/10.1038/ngeo2521

Yuan, H., & Romanowicz, B. (2010). Lithospheric layering in the North American Craton. *Nature*, *466*(7310), 1063–1068. https://doi.org/10.1038/nature09332

Zhao, J., McCulloch, M. T., & Korsch, R. T. (1994). Characterisation of a plume-related approximately 800 Ma magmatic event and its implications for basin formation in central-southern Australia. *Earth and Planetary Science Letters*, *121*(3–4), 349–367. https://doi.org/10.1016/0012-821X(94)90077-9